Lawrence Berkeley National Laboratory

Title
Nano-FTIR Investigation of the CM Chondrite Allan Hills 83100

Permalink
https://escholarship.org/uc/item/0x13q13w

Journal
Journal of Geophysical Research Planets, 127(5)

ISSN
2169-9097

Authors
Young, JM
Glotch, TD
Yesiltas, M
et al.

Publication Date
2022-05-01

DOI
10.1029/2021je007166

Peer reviewed

Nano-FTIR Investigation of the CM Chondrite Allan Hills 83100

J. M. Young[1], T. D. Glotch[1] , M. Yesiltas[2] , V. E. Hamilton[3] , L. B. Breitenfeld[1] , H. A. Bechtel[4], S. N. Gilbert Corder[4] , and Z. Yao[4,5]

[1]Department of Geosciences, Stony Brook University, Stony Brook, NY, USA, [2]Faculty of Aeronautics and Space Sciences, Kirklareli University, Kirklareli, Turkey, [3]Southwest Research Institute, Boulder, CO, USA, [4]Advanced Light Source, Lawrence Berkeley National Laboratory, Berkeley, CA, USA, [5]Department of Physics and Astronomy, Stony Brook University, Stony Brook, NY, USA

Abstract Mid-infrared (MIR) spectroscopy has been used with great success to quantitatively determine the mineralogy of geologic samples. It has been employed in a variety of contexts from determining bulk composition of powdered samples to spectroscopic imaging of rock thin sections via micro-Fourier transform infrared (micro-FTIR) imaging spectroscopy. Recent advances allow for IR measurements at the nanoscale. Near field nanoscale infrared imaging and spectroscopy with a broadband source (nano-FTIR) enable understanding of the spatial relationships between compositionally distinct materials within a sample. This will be of particular use when analyzing returned samples from Bennu and Ryugu, which are thought to be compositionally like CI or CM1/2 carbonaceous chondrites. Returned samples will likely contain olivine/pyroxene chondrules that have been transformed into hydrous phyllosilicates, sulfides, carbonates, and other alteration phases. The use of near-field infrared techniques to probe the boundaries between once pristine chondrules and alteration phases at the nanoscale is a novel approach to furthering our understanding of the compositional evolution of carbonaceous asteroids and the processes that drive their evolution. Here we report the results of nano-FTIR spectroscopy and imaging measurements performed on the carbonaceous chondrite Allan Hills (ALH) 83100 (CM1/2). We show with nanoscale resolution that spatially resolved Fe-Mg variations exist within the phyllosilicates around a chondrule rim. We also present effects of crystal orientation on the nano-FTIR spectra to account for the spectral differences between the meteorite and mineral spectra.

Plain Language Summary National Aeronautics and Space Administration's OSIRIS-REx mission will return a sample of near-Earth asteroid Bennu to Earth in September 2023. Based on remote sensing analyses of the asteroid, it is expected that the sample will be similar to CI or CM chondrite meteorites. Key remote sensing analyses of Bennu included thermal infrared emission spectroscopy. In this work, we conduct infrared spectral analyses of Allan Hills (ALH) 83100, a CM1/2 chondrite that shares spectral similarities to Bennu. We use synchrotron near-field infrared nano-infrared (nano-IR) measurements to analyze the sample at scales of about 30 nm/pixel. This allows us to capture the spectra of very fine-grained components in meteorites that contribute to their overall bulk spectra measured from remote sensing platforms. While nano-IR spectra do not directly translate to remote-sensing infrared measurements, identification of mineral and organic components in analog extraterrestrial materials provides key constraints on models of Bennu's composition from orbital infrared spectroscopy. We document the chemical alteration of a chondrule and show strong alteration gradients in the sample over length scales smaller than 10 microns. The variability in Fe and Mg in the phyllosilicate-rich matrix of the meteorite over small spatial scales may indicate aqueous alteration in the ALH 83100 parent body as well as in the solar nebula.

1. Introduction

Mid-infrared (MIR) spectroscopy has been used to great success toward quantitatively determining the mineralogy of geologic samples (Clark & Roush, 1984; Hapke, 1981; Hunt & Salisbury, 1970; Johnson et al., 1983; King & Ridley, 1987; Mustard & Pieters, 1987). It has been employed in a variety of contexts from determining bulk composition of powdered samples (Friedlander et al., 2015; Lane et al., 2011; Shirley & Glotch, 2019) to spectroscopic imaging of rock sections via micro-Fourier transform infrared (micro-FTIR) (Farrand et al., 2016, 2018; Jaret et al., 2015, 2018; Johnson et al., 2020; Yesiltas et al., 2019; Yesiltas & Kebukawa, 2016).

The spatial resolution of MIR spectroscopic measurements has typically been limited by the diffraction limit of light, resulting in minimum spot sizes of ~1 μm at synchrotron facilities with bright infrared light sources (Nasse et al., 2011; Yesiltas et al., 2017). In their seminal paper, Amarie et al. (2009) demonstrated the first continuous infrared spectroscopic measurements at nanoscale (~20 nm) resolution, achieved by coupling an FTIR spectrometer with a scanning near field optical microscope (SNOM), the latter of which had already demonstrated nm resolution in the visible wavelength range (Dürig et al., 1986).

The advent of near-field infrared (nano-FTIR) spectroscopy and imaging has allowed for measurement of the vibrational spectra of material monolayers and even single molecule complexes (Amenabar et al., 2013; Xu et al., 2012). The ability to make high signal-to-noise ratio (SNR) measurements at high spatial resolutions makes the nano-FTIR technique an excellent method of analysis when sample availability is low or scientific questions to be addressed require high spatial resolution. This makes nano-FTIR an extremely effective tool for the study of extraterrestrial planetary materials. Dominguez et al. (2014) used nano-FTIR to study the chemistry of a single cometary dust grain from Comet 81P/Wild 2, collected during NASA's Stardust mission. Others have used nano-FTIR to understand nano-scale mineral and organic compositional variation in carbonaceous and ordinary chondrites, resulting from various parent body alteration processes (Glotch et al., 2019; Kebukawa et al., 2019; Yesiltas et al., 2020, 2021).

The nano-FTIR method, and the previous works that have employed its use, will be of particular use when analyzing returned samples of the near-Earth asteroids Bennu and Ryugu from the OSIRIS-REx and Hayabusa-2 missions respectively (e.g., Dominguez et al., 2022; Mathurin et al., 2022). Both of these C-type asteroids are thought to be compositionally analogous to the CI or CM2 carbonaceous chondrites (King et al., 2015; Kitazato et al., 2019), which have undergone varying degrees of aqueous alteration. Recent results have confirmed hydrated and volatile-rich bulk composition of Bennu as well as the linkage between Bennu and carbonaceous chondrites (Lauretta et al., 2019). Returned samples will likely contain organics, phyllosilicates, carbonates, and other alteration phases (Breitenfeld et al., 2021; Hamilton et al., 2019, 2021; Kaplan et al., 2020). The use of near-field infrared techniques to probe the boundaries between once pristine chondrules and alteration phases at the nanoscale is a novel approach to further improving our understanding of the compositional evolution of carbonaceous asteroids and the processes that drive their evolution.

Furthermore, the use of nano-FTIR imaging and spectroscopy is an excellent tool for understanding organic molecules found within carbonaceous chondrites and asteroid samples, including the identity of those compounds and the spatial relationships between organic compounds and mineralogical phases (Takir et al., 2013; Yesiltas et al., 2013, 2021). This information may prove critical to understanding how complex organic compounds found in meteorites and asteroid samples formed (Pearson et al., 2002; Simon et al., 2020). To that end, here, we report the results of nano-FTIR spectroscopy and imaging measurements performed on the carbonaceous chondrite ALH 83100 (CM1/2), a potential compositional analog for the asteroid Bennu.

Directly relating nano-IR spectra of extraterrestrial materials with macroscopic remote sensing measurements of solar system objects remains a challenge, as the strong interaction between the nano-IR probe and the sample typically results in distortions and shifts of spectral features to longer wavelengths compared to traditional far-field IR spectra (Dominguez et al., 2014; Hillenbrand et al., 2002). Several theoretical frameworks have been developed to model the near-field interaction of the nano-IR probe and the sample, enabling the extraction of the complex refractive indices (optical constants) of the sample material (e.g., Amarie & Keilmann, 2011; Averbukh et al., 2000; Chui et al., 2018; Cvitkovic et al., 2007; Hillenbrand & Keilmann, 2000; Jiang et al., 2016; McLeod et al., 2014). While beyond the scope of this work, extracted nano-IR optical constants, in combination with a light scattering model (e.g., Hapke, 1981; Shkuratov et al., 1999), could be used to directly relate extraterrestrial returned samples to remote infrared measurements of their parent bodies and other solar system objects.

2. Materials and Methods

2.1. Petrographic Imaging

A reflected light mosaic of the ALH 83100 thin-section sample was formed by "stitching" together individual microscopy images using the software PtGUI. Individual images used to create mosaics were captured using a Fein Optic microscope with a 4x objective lens and an AM-Scope MU1403 camera attachment.

2.2. Micro-FTIR Hyperspectral Imaging

We collected a hyperspectral micro-FTIR reflectance map of ALH 83100 using a Nicolet iN10MX imaging spectrometer in the Center for Planetary Exploration at Stony Brook University. The instrument is equipped with a 16-pixel MCT linear array detector (a 1-dimensional focal plane array) and a sample stage that moves perpendicular to the long dimension of the detector array to build up hyperspectral images over the $\sim$4,000–500 cm^{-1} (2.5–20 μm) range. The micro-FTIR image cube has a fixed spatial resolution of 25 μm per pixel and a spectral resolution of 4 cm^{-1}. We measured a gold standard for calibration of the collected micro-FTIR data. To display compositional variation across the sample, we utilized spectral indices (wavenumbers, spectral channels, and band depths) to map the band strengths of the 3 μm ($\sim$3,300 cm^{-1}) OH/H$_2$O feature, the $\sim$2.7 μm ($\sim$3,700 cm^{-1}) OH feature, and the $\sim$7 μm ($\sim$1,430 cm^{-1}) CO$_3$ feature. The most widely used and simplest method to parameterize the presence and strength of spectral bands is a band depth index (e.g., Clark & Roush, 1984; Viviano-Beck et al., 2014). The band strength (B) is calculated as the ratio of the peak center maximum, C, at frequency ν_C, to C*, the phase value on the continuum between points L and H, located at frequencies ν_L and ν_H, respectively. Mathematically, $\boldsymbol{B} = 1 - \frac{C^*}{C} = \frac{aL+bH}{C}$ where $\boldsymbol{a} = 1 - \boldsymbol{b}$ and $\boldsymbol{b} = \frac{\nu_C - \nu_L}{\nu_H - \nu_L}$. In practice, to increase index consistency in a spectrum that may contain noise, the values of C, C*, L, H, ν_L, ν_C, and ν_H may be averages of two or more spectral channels.

2.3. Nano-FTIR Spectroscopy

We acquired nano-FTIR measurements at the Synchrotron Infrared Nano Spectroscopy (SINS) beamline at the Advanced Light Source (ALS) at Lawrence Berkeley National Laboratory (LBNL) (Bechtel et al., 2020). We collected both near-field infrared images at discrete wavelengths and point spectra of a polished thin-section ($\sim$30 μm thickness) of the CM2 chondrite Allan Hills (ALH) 83100. Spectra were collected using a neaspec neaSNOM near field system coupled with a conductive atomic force microscope (AFM) tip for focusing the synchrotron infrared beam source (Amarie et al., 2009; Bechtel et al., 2020). Scattering-type near-field phase and amplitude spectra referenced to a gold standard were collected at harmonics of the AFM tapping frequency. Far-field contributions to the acquired signal are removed by demodulating the signal at higher harmonics of the tapping frequency (n $\geq$ 2) (Hillenbrand & Keilmann, 2000; Labardi et al., 2000). Second harmonic (n = 2) data are presented here as a good compromise between near-field signal and background suppression. Demodulation of the initial signal produces both an amplitude and a phase spectrum. These spectra are approximately analogous to the reflectance and absorbance spectra of typical far-field FTIR measurement (Bechtel et al., 2020), respectively. As such, we will make frequent comparisons between amplitude-reflectance and phase-absorbance in this work. It should be noted that the strong electromagnetic interaction between the AFM tip and the sample surface can distort the shapes and positions of the major vibrational features, sometimes making direct comparisons difficult. Nano-IR spectral peaks are typically shifted to lower frequencies compared to far-field IR features. While the size of the shift generally dependent on the strength of the feature, shifts are typically on the order of $\sim$15 cm^{-1} (Dominguez et al., 2014; Hillenbrand et al., 2002). The spatial resolution of point spectroscopy measurements is controlled by the radius of curvature of the AFM tip, which is <20 nm. Collected spectra have $\sim$8 cm^{-1} spectral sampling.

For imaging, we used the same neaspec instrument operating in pseudo-heterodyne (a background suppression method) imaging mode with two tunable lasers centered $\sim$1,666 cm^{-1} and $\sim$1,000 cm^{-1} respectively. As water has an absorption at $\sim$1,600 cm^{-1} (H-O-H bending), we used the 1,666 cm^{-1} laser to examine the spatial distributions of hydrated mineral phases within the sample. Measurements made with the 1,666 cm^{-1} laser were at the discrete 1,675, 1,623, and 1,572 cm^{-1} wavenumbers, while measurements made with the 1,000 cm^{-1} laser were taken at the 1081, 1039, 944, and 935 cm^{-1} wavenumbers. We chose the 1,000 cm^{-1} laser to understand spectral variations of the prominent Si-O vibrational feature characteristic of silicate minerals. Scanned image area dimensions were 11 × 11 μm, and collected images had dimensions of 550 pixels × 550 pixels, yielding an image resolution of 20 nm/pixel. The integration time was 7 ms at each spot, yielding a collection time of $\sim$35 min per image. Like the point spectra, phase and amplitude maps were collected at the tapping frequency of the AFM tip ($\sim$300 kHz).
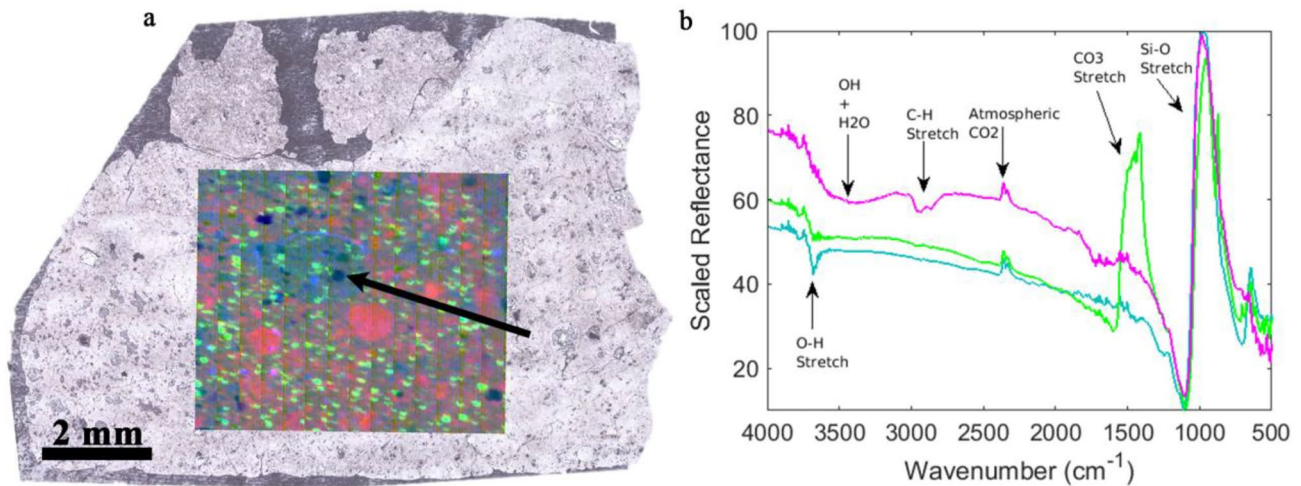
Figure 1. (a) RGB composite micro-Fourier transform infrared (micro-FTIR) map collected from Allan Hills 83100 overlain on a corresponding reflected light microscopy image mosaic; Black arrow points at the chosen target chondrule shown as a dark blue circle. (b) Scaled micro-FTIR reflectance spectra containing the spectral features to which the RGB pixels of the micro-FTIR hyperspectral map are tied: The pink spectrum contains a strong C-H stretch feature (organic carbon), the green spectrum contains a strong CO_3 stretch feature (carbonate phases), and the blue spectrum contains a strong O-H stretch feature (hydrous minerals).

2.4. Sample and Sampling Location

ALH 83100 is a type 1/2 CM Antarctic meteorite find with a weathering grade of Be, meaning that the presence of moderate rusting and evaporate minerals caused by terrestrial weathering are observed on this sample. It is slightly more hydrated than conventional CM2 chondrites (Zolensky et al., 1997), hence the classification of CM1/2. ALH 83100 is composed of ∼85% hydrous phyllosilicates and contains minor abundances (<3 wt. %) of magnetite, sulfates, and calcite respectively (Hanna et al., 2020; Howard et al., 2011). It has been extensively altered by aqueous activity (De Leuw et al., 2009). 1.9 wt.% C was identified in ALH 83100 by Alexander et al. (2013). It is composed of ∼0.76 wt. % insoluble organic material (IOM), in which several amino acids have been detected (Alexander et al., 2007; Elsila et al., 2012). Another 8–9 wt. % of ALH 83100 is made up of the primary ferromagnesian silicate phases olivine and pyroxene in the form of chondrule grains and chondrule fragments. Its carbonate abundance is ∼2.8 vol% (De Leuw et al., 2010). For this work, a polished thin section (∼30 μm thickness) of ALH 83100 was loaned from the US Antarctic Meteorite collection at Johnson Space Center (JSC). In this sample, we chose to target the interface between one such chondrule and the surrounding fine-grained matrix. This boundary zone was targeted because it might provide information regarding the aqueous alteration of the primary chondrule minerals into the hydrous phyllosilicate alteration products in the surrounding matrix.

The reflected light microscopy and micro-FTIR composite images of ALH 83100 are shown in Figure 1. The colors shown in the RGB image are representative of common features observed in the spectra of the hyperspectral map image: red represents a relatively strong C-H stretch absorption (e.g., Yesiltas & Kebukawa, 2016), green represents a CO_3 (carbonate) stretch reflectance feature (e.g., Lane & Christensen, 1997), and blue represents a strong O-H stretch absorption feature (e.g., Miyamoto & Zolensky, 1994). Measurements were collected in an environment purged with dry air, ensuring that OH and H_2O spectral features are due to the sample and not the ambient atmosphere. Spectra containing O-H stretch features likely represent serpentine minerals, which are hydroxylated phyllosilicates that are common in CM chondrites. These indicate aqueous alteration, making blue zones of particular interest. Based on the prominence of hydroxylated mineral signatures, we chose the chondrule indicated by the arrow in Figure 1a. This chondrule displays strong O-H stretch features and is also bordered by material that is both faintly red and blue in the hyperspectral image. This suggests that the outlying matrix contains hydrous minerals but also organic carbon. Numerous cracks are seen throughout the chondrule (Figure 2). Rather than collect nano-FTIR measurements from these areas, we chose the "northern" chondrule-matrix interface zone as the measurement area of interest to maximize the compositional variability within the scene. The imaged region includes areas of both chondrule and fine-grained matrix exposure compared to the slivers of matrix in
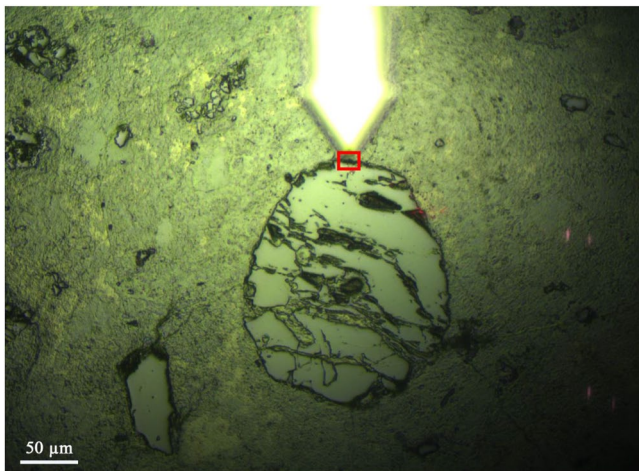
Figure 2. Reflected light microscopy image of the target chondrule; The measurement collection area is the interface between the chondrule and outlying fine-grained matrix, as indicated by the red box at the end of the atomic force microscope cantilever.

the chondrule interior. Our goal was to capture information regarding the spectral variability of these visibly different types of materials as well as differences between chondrule and matrix.

Nano-FTIR imaging allows simultaneous collection of sample topography with IR images. The collected topographic map shows a high resolution view of the region of interest (Figure 3a) and clearly delineates the boundary zone of interest between the chondrule and the outlying matrix. The chondrule edge, in the bottom quarter of the map, has relatively high elevation compared to that of the outlying matrix, which makes up the majority of the scan. The low-lying matrix, shown in shades of dark gray in Figure 3a, contains areas of higher topography. In general, there is some height difference (<1 μm) between the chondrule grain and the fine-grained matrix area.

3. Results

3.1. Single Wavelength Nano-IR Images

We collected nano-FTIR images of the selected area of interest at wavelengths of 5.97, 6.16, 6.36, 9.25, 9.62, 10.18, and 10.59 μm (1675, 1623, 1572, 1081, 1039, 944, and 935 cm^{-1}). These wavelengths were chosen to bound and sample the fundamental mid-IR H$_2$O and Si-O vibrational modes. All optical amplitude images shown here are second harmonic optical amplitude images that were each referenced to a separate standard. Beginning with the 1675 cm^{-1} map (Figure 3b.), striking compositional variability is observed. The chondrule edge is divided into two section: the bottom left portion, which is largely a high amplitude zone and the area in the right corner of the map, which has the lowest amplitudes of the map. The 1675 cm^{-1} optical amplitude of the matrix also varies spatially. High amplitude zones border the chondrule grain, while the top of the map is characterized by broadly low amplitude zones. The area between these relatively homogenous regions of matrix
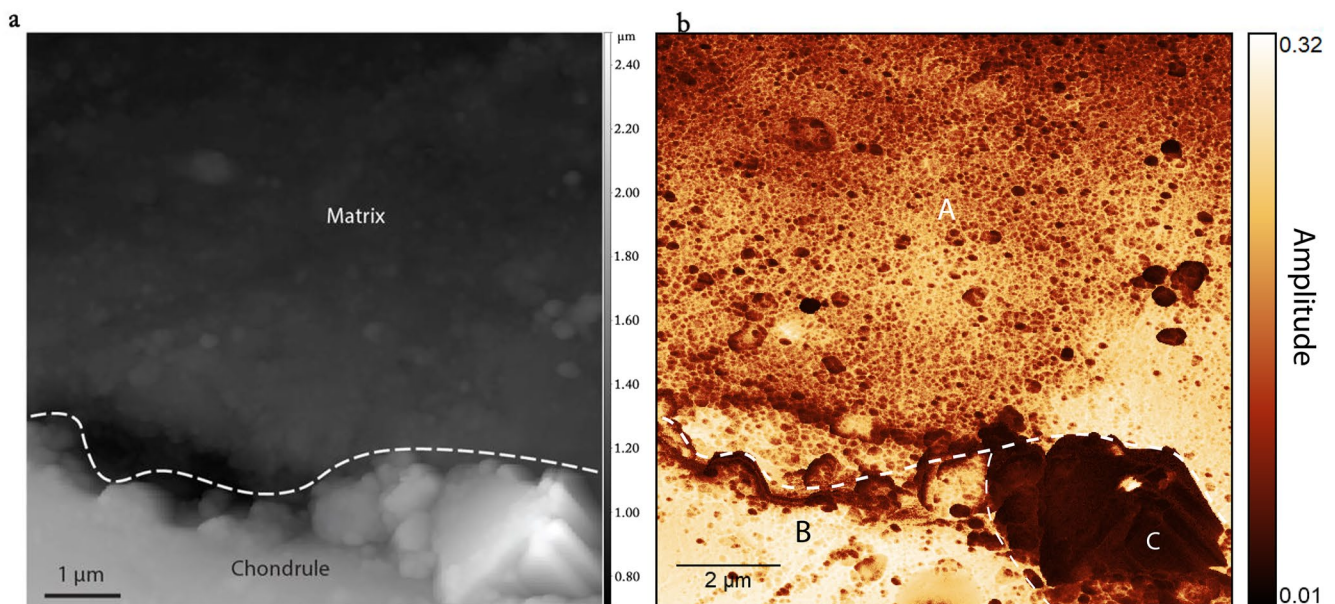
Figure 3. (a) Topography map of the chondrule-matrix interface area of interest; white pixels represent locally high topography and black pixels represent locally low topography; Dashed line roughly delineates the boundary between the chondrule grain and surrounding matrix; The chondrule grain (bottom-quarter) has relatively high topography compared to the outlying matrix. (b) 1675 cm^{-1} spectral map of chondrule-matrix interface region of interest; Pixel color represents the amplitude of the second atomic force microscope tapping harmonic frequency; Horizontal dashed line shows the chondrule-matrix boundary; Vertical dashed line shows the boundary between the two chondrule zones. Zones A, B, and C represent respectively the outlying matrix, the left portion of the chondrule, and the bottom corner portion of the chondrule.

Figure 4. (top row) (1,623 cm^{-1} and 1,527 cm^{-1} maps of chondrule-matrix interface region of interest; (middle row) 1,081 cm^{-1} and 1,039 cm^{-1} maps of chondrule-matrix interface region of interest; (bottom row) 982 cm^{-1} and 944 cm^{-1} maps; Horizontal dashed line shows the chondrule-matrix boundary; Vertical dashed line shows the boundary between the two chondrule zones. Zones A, B, and C represent respectively the outlying matrix, the left portion of the chondrule,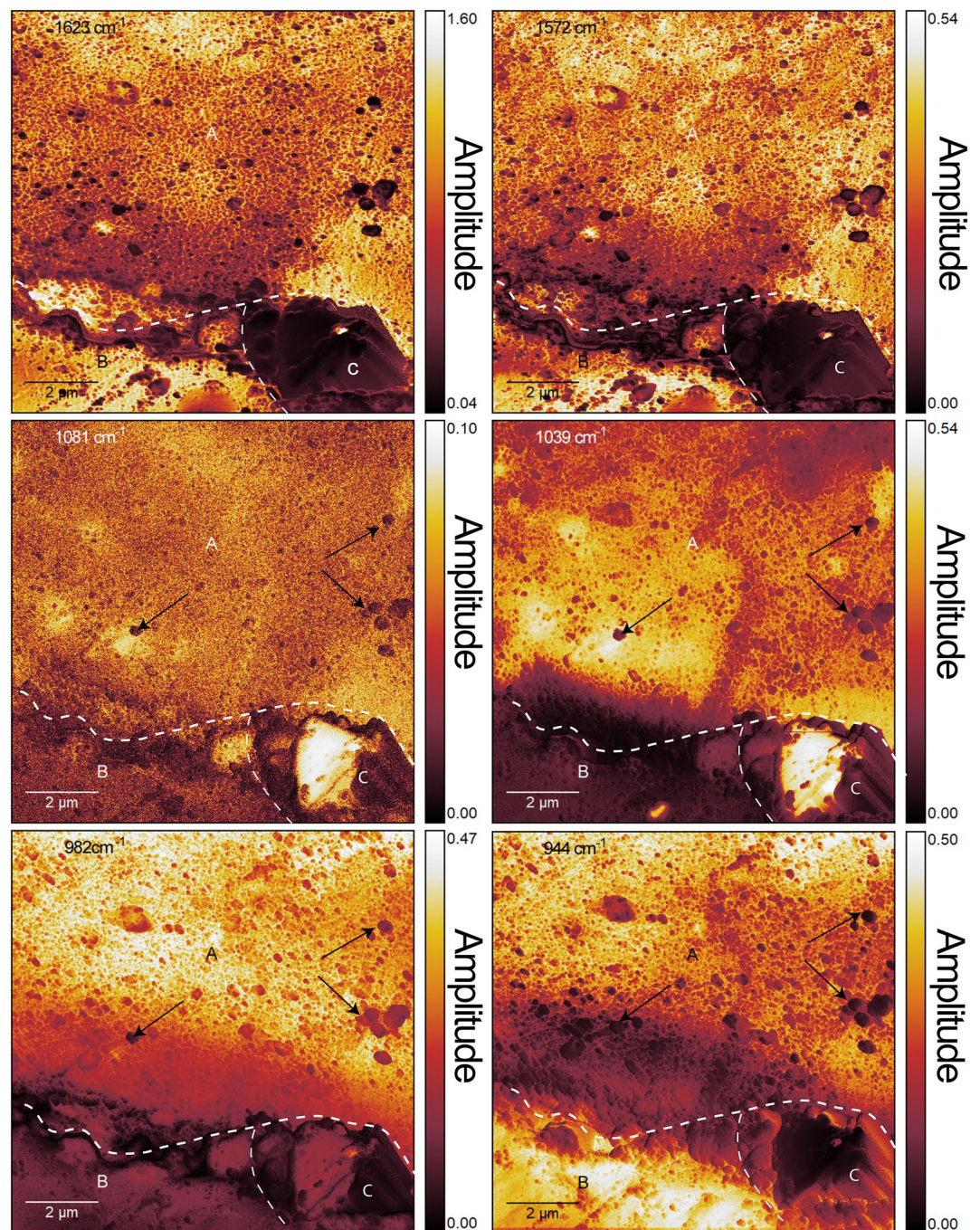 and the bottom corner portion of the chondrule. Pixel color represents the relative optical amplitude of the second atomic force microscope tapping harmonic frequency; Black arrows indicate "grains" suspended in the matrix with low optical amplitude values.

is characterized by the optical amplitude that varies at a spatial scale of <0.1 μm. Features with radii <0.5 μm are frequent in this region; these grains are generally low optical amplitude, but still vary. Intra-chondrule variation exists at 1,623 and 1,571 cm^{-1} as well (Figure 4.). The relationship between the distinct zones of the exposed chondrule edge are maintained at these frequencies: the left portion has relatively higher optical amplitudes

and the right portion has the lowest optical amplitude pixels of the map. At both 1,623 and 1,571 cm^{-1}, the left portion of the chondrule appears less homogenous than at 1,675 cm^{-1}. The left portion of the chondrule edge has relatively lower optical amplitude at these frequencies than at 1675 cm^{-1}. The edge of the chondrule is better defined at these frequencies as well; the border is much lower optical amplitude than the surrounding matrix at 1,623 and 1,571 cm^{-1} than at 1,675 cm^{-1}. At 1,623 and 1,571 cm^{-1}, the mottled or web like amplitude variation seen in the matrix at 1,675 cm^{-1} is even more prevalent. The spectral contrast between the outlying grains and the fine-grained matrix, in which they are suspended, is also more pronounced.

At 1,081 and 1,039 cm^{-1}, intra-chondrule optical amplitude variation still exists (Figure 4.) The left portion of the chondrule exposure is homogenously low optical amplitude at both wavelengths. In contrast, a part of the bottom right portion of the chondrule is very high optical amplitude at both wavelengths. At 1,081 cm^{-1}, the outlying fine-grained matrix is largely homogenous with a low optical amplitude but does still exhibit weak nano-scale mottled variation. Suspended grains (black arrows) also have low optical amplitude values at this wavelength. At 1,039 cm^{-1}, the matrix is less homogenous with enclaves of high optical amplitude material and more extensive nano-scale mottling. The small outlying grains are generally lower optical amplitude than the surrounding matrix at 1,039 cm^{-1}.

At 982 cm^{-1}, intra-chondrule variation, observed at other frequencies, has disappeared (Figure 4). Instead, the whole chondrule exposure is characterized by low optical amplitude values. At this wavelength, the fine-grained matrix can be described as two homogenous zones: (a) the middling amplitude border zone (b) the high amplitude outer region. As the name implies, the border portion of observed matrix, which immediately borders the chondrule and extends outward for ∼1–2 μm radially, has median amplitude values. These values increase as distance from the chondrule grain increases. The outer region of matrix is homogenously high optical amplitude material at this wavelength. Observed variation in this region is caused by the low optical amplitude of the small, suspended grains. At 944 cm^{-1}, intra-chondrule variation returns, with the left portion of the chondrule exposure displaying high optical amplitude values and the bottom right zone having low optical amplitude pixels. There is also widespread variability within the matrix at this wavelength. The matrix border region again has moderate optical amplitude values and is relatively homogenous. Higher optical amplitude pixels and nanoscale amplitude mottling characterize the outer matrix region. The matrix suspended grains all appear to have low optical amplitude values at this wavelength.

3.2. Multispectral Nano-IR Map

Using the map data collected at three discrete wavelengths, we generated a decorrelation stretched (DCS; Gillespie et al., 1986) false-color image that provides a clearer picture regarding the compositional variability in this portion of the sample. The color channels of the DCS map, R, G, and B represent 944, 1,039, and 1,081 cm^{-1}, respectively. The exact data used to create the DCS maps were individual second harmonic phase maps for each wavelength, meaning that the color of a pixel is tied to the phase value of its counterpart pixel from each relevant amplitude map. The DCS map (Figure 5) shows which areas of the map are spectrally similar and dissimilar, and corroborates observations of the individual amplitude maps. There is widespread spectral variability within the chondrule grain, within the matrix, and between the chondrule and matrix. The composite map displays the spectral contrast between the left portion of the chondrule exposure and the bottom right zone. In the composite map, the bottom left is shown in yellow and orange while the bottom right is mainly blue. The edge regions of the chondrule have coloring of pinks and red, distinguishing themselves from the more interior portions of the grain. The fine-grained matrix shown in Figure 5 is green, suggesting a maximum optical amplitude around 1,039 cm^{-1}, with minor variations in color and brightness. The observed small grains suspended in the fine-grained matrix vary in color, between orange, pink and blue, suggesting substantial spectral variability. Interestingly, this map also reveals a long vein like structure (white arrows), which had been obscured in the individual optical amplitude maps. This structure extends out radially from the chondrule exposure for ∼8 μm and has a width of 0.25–0.33 μm.

On the basis of spectral variability observed in the individual optical amplitude images and the false color DCS map, we collected point spectra from various positions within the area of interest. The positions from which the point spectra were collected can be seen in Figure 5. These point spectra were collected from areas that belong
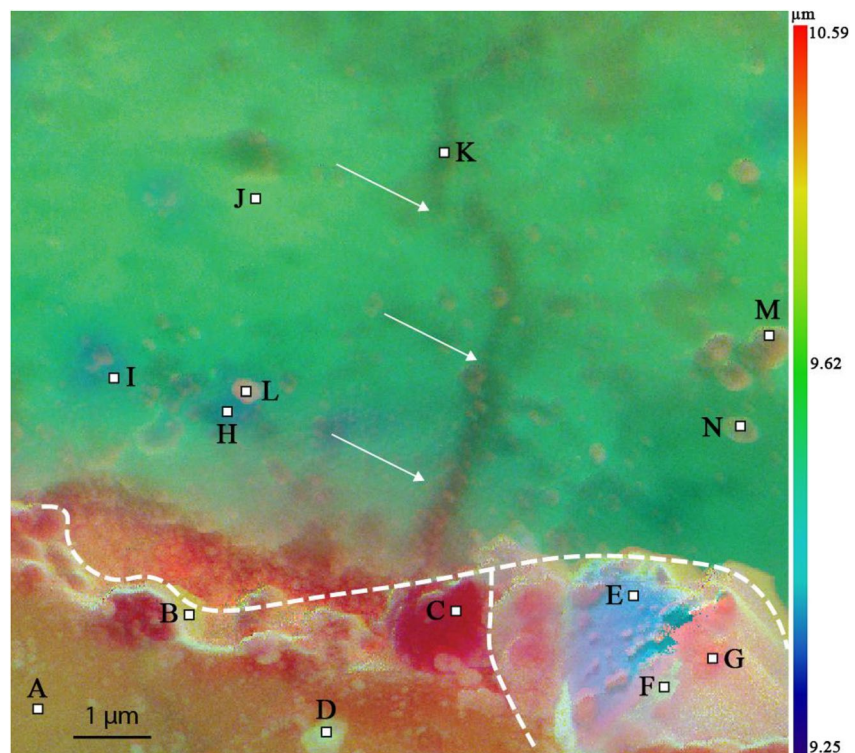
Figure 5. False color RGB image composite of the chondrule-matrix area of interest; R, G, and B color channels represent 944, 1,039, and 1,081 cm^{-1}, respectively. Black edged squares represent positions where single spectra were collected. Arrows point to vein-like structure; Horizontal dashed line shows the chondrule-matrix border; Vertical dashed line shows border between chondrule zones; Points A, B, C, and D lie within the left chondrule zone; Points E, F, and G lie within the bottom right corner chondrule zone; Points H, I, J, K, L, M, and N lie within the matrix zone.

to four categories: the left portion of the chondrule exposure, the bottom right corner zone of the chondrule, the fine-grained matrix, and the grains suspended in the matrix.

3.3. Nano-IR Spectra

We collected spectra from four positions, A, B, C, and D, within the left portion of the chondrule exposure (Figure 6). Amplitude spectrum C is relatively flat but has noticeable a broad maximum centered at 1050 cm^{-1}. Spectrum A, by contrast, has a prominent amplitude maximum at 890 cm^{-1} and several smaller features at 830, 950, and 970 cm^{-1}. Spectrum D also has a broad amplitude maximum centered around 890 cm^{-1}, with additional features at 950 and 970 cm^{-1}.

Phase spectra show that A and D have similar spectral profiles. They both have a triplet with bands at 920, 960, 985 cm^{-1}. Spectrum B has a different profile. It presents prominent bands at 950 and 990 cm^{-1} and a smaller feature at 1,000 cm^{-1}. Similar to the amplitude spectrum, the phase spectrum of C contains relatively weak features but bands at 927, 953 and 985 cm^{-1} are still visible.

From the bottom corner zone of the chondrule exposure, we collected spectra from three positions: E, F, and G. The amplitude spectrum of point E (Figure 7.) shows one prominent maximum centered at 1,030 cm^{-1} and an ancillary feature at 970 cm^{-1}. Spectrum F has amplitude peaks at the same positions as spectrum E, but with lower overall amplitudes. The amplitude spectrum of point G has less intense features. Their corresponding phase spectra are noiser. Spectrum E has a broad peak with maxima at 1,100 cm^{-1} and extends up to 1,400 cm^{-1}. Spectra F and G have a maxima at 1,082 and 1,055 cm^{-1} respectively. As in the amplitude spectra, these broad bands have decreasing intensity as well, with spectrum E having the most intense peak.
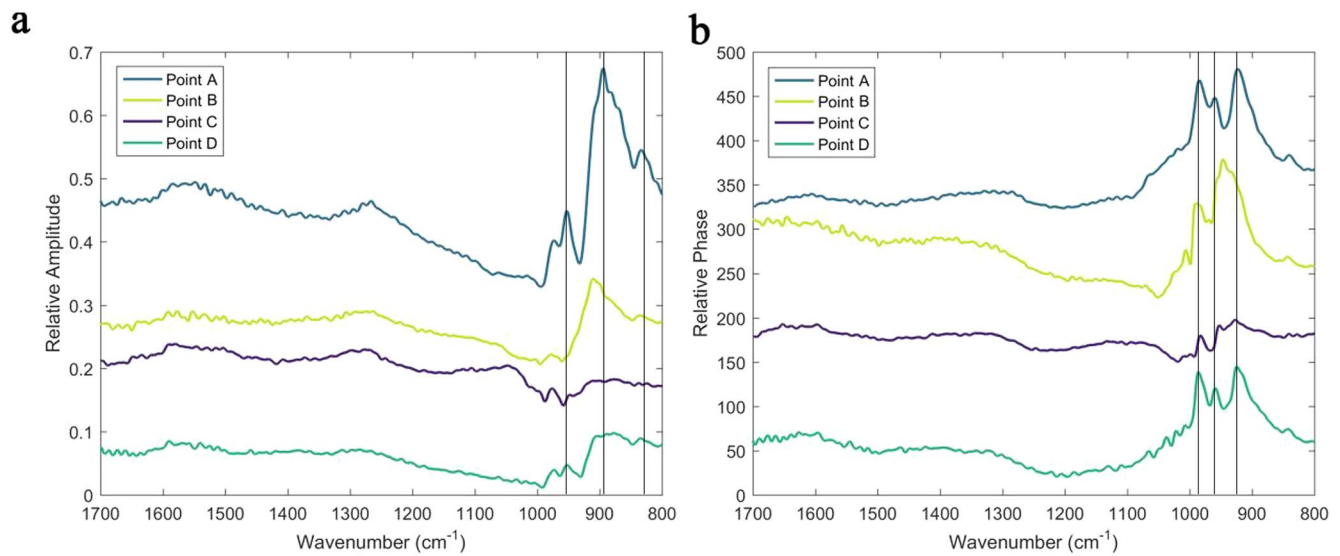
Figure 6. Nano-Fourier transform infrared (a) amplitude and (b) phase spectra collected from the left portion of the chondrule exposure. Amplitudes and phases are relative and spectra have been offset for comparison.

We collected additional spectra, shown in Figure 8, from four positions in the outlying fine-grained matrix: H, I, J, and K. The amplitude spectrum of Point H has two amplitude maxima at 970 and 1,020 cm^{-1} and a third broad maximum centered at ~850 cm^{-1}. Spectrum K has a single broad maximum centered around 960 cm^{-1}, and spectrum J has the same feature with an overall higher amplitude. Spectrum I has a prominent amplitude maximum at 1,030 cm^{-1} and a smaller feature at 970 cm^{-1}. The phase spectra of these points present a prominent and well-defined peak near 1,040 cm^{-1}. Spectra I and H additionally present a weaker band at 980 cm^{-1}, which is not resolved in spectra K and J.

Finally, three spectra were collected from positions on grains suspended in the fine-grained matrix: L, M, and N (Figure 9). Amplitude spectrum L has amplitude maxima at 970 and 1,020 cm^{-1}. Spectrum M also has two maxima at 970 cm^{-1}, the other at 1,000 cm^{-1}. Finally, spectrum N is relatively flat, but has a broad maximum centered at 980 cm^{-1}. Their corresponding phase spectra present a broad symmetric band centered around 1,030–
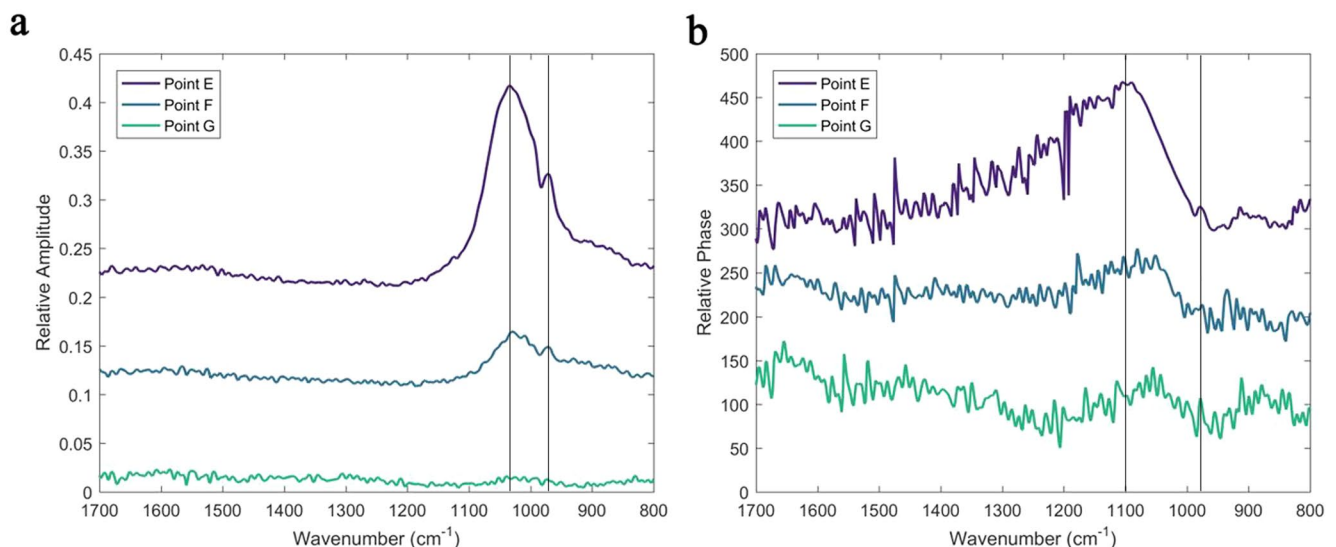

Figure 7. Nano-Fourier transform infrared (a) amplitude and (b) phase spectra collected from the bottom corner zone of the chondrule exposure. Amplitudes and phases are relative and spectra have been offset for comparison.
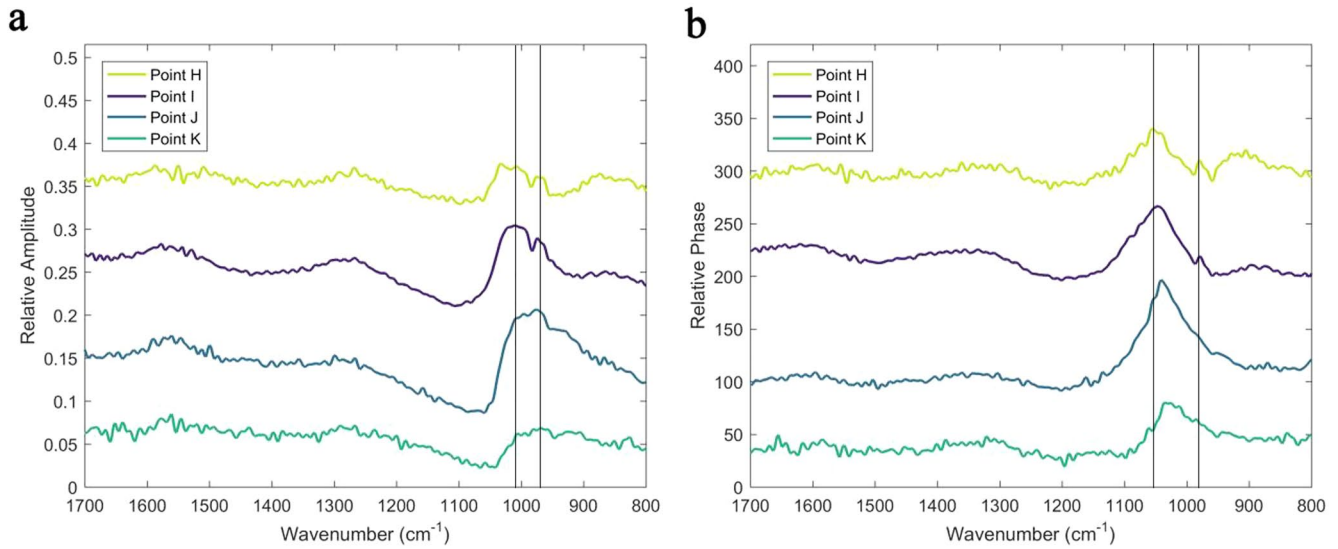
Figure 8. Nano-Fourier transform infrared (a) amplitude and (b) phase spectra collected from the fine-grained matrix of the region of interest. Amplitudes and phases are relative and spectra have been offset for comparison.

1,050 cm^{-1}. A smaller feature at 978 cm^{-1} and a broad bump at 896 cm^{-1} are also present in spectrum L. We note that most of the spectra presented here also have a broad feature near 1,275 cm^{-1}.

4. Discussion

We place the point spectra, described in the results section, into two main groups. The spectra collected from member positions of a given group share similar feature positions and overall line shapes, in both their amplitude and phase spectra. This suggests that the materials represented by the positions/point spectra of a group are compositionally similar. We also define a third group containing points with flat and featureless spectra. These are likely sulfides or oxides with long wavelength spectral features that fall outside the range of our measurement capabilities. Points E and N belong to this group and are omitted from discussion.
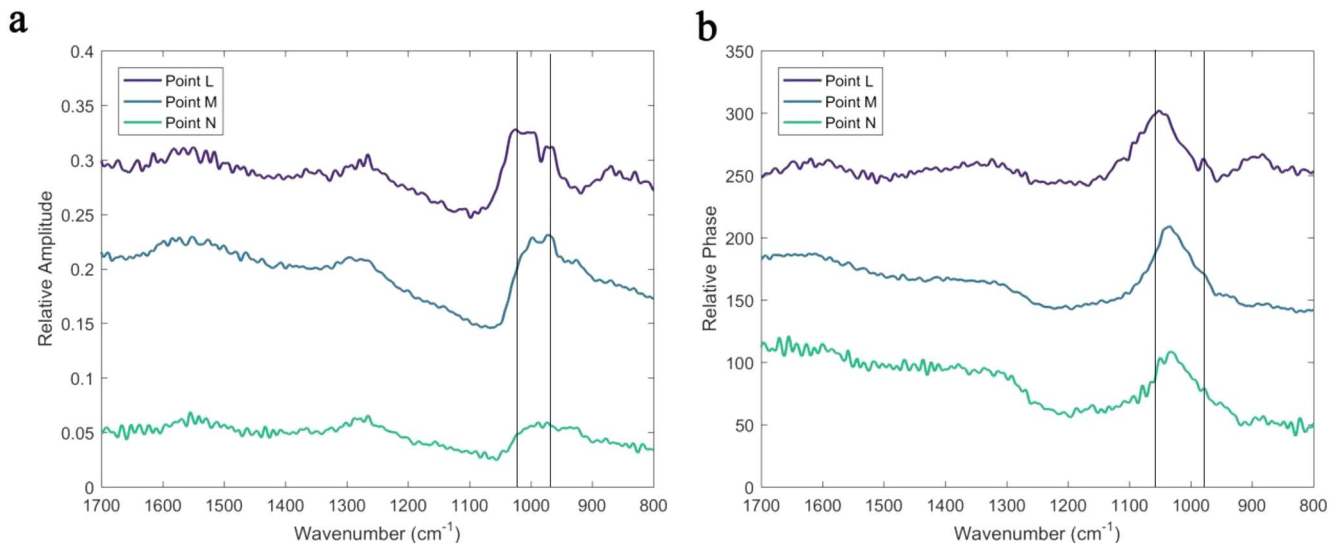

Figure 9. Nano-Fourier transform infrared amplitude (a) and (b) phase spectra collected from grains suspended in the fine-grained matrix zone of the region of interest. Amplitudes and phases are relative and spectra have been offset for comparison.
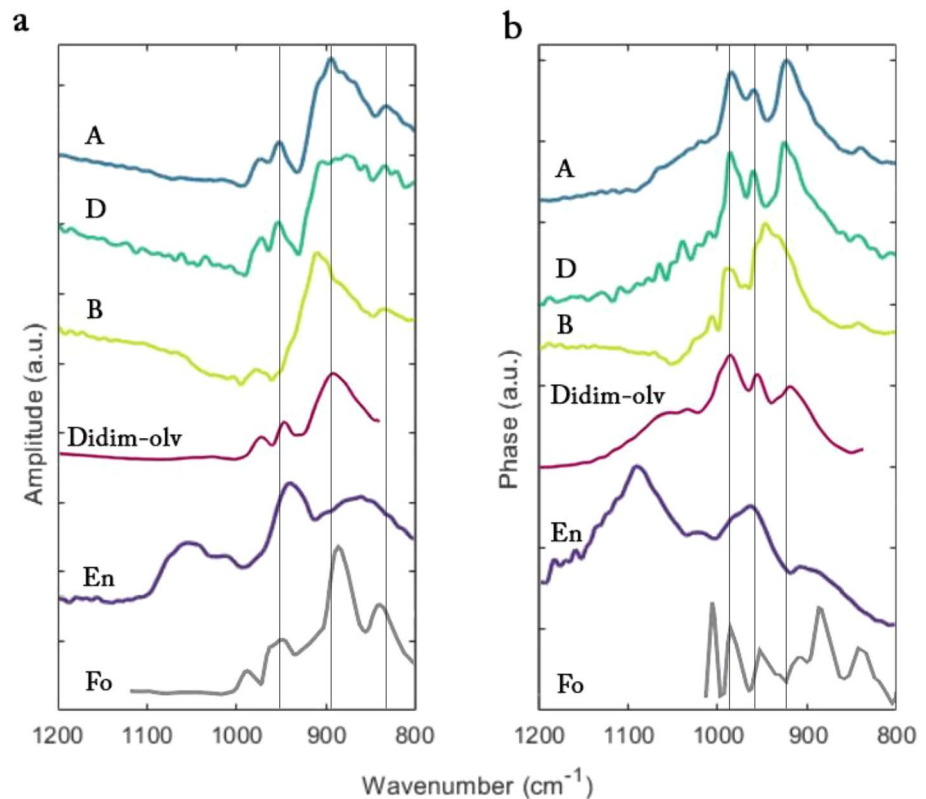
Figure 10. (a) Amplitude and (b) phase spectra of points A, D and B with amplitude spectra of single crystal enstatite (En) and forsterite (Fo); Enstatite spectra are from this study; forsterite spectra taken from Dominguez et al. (2014). Olivine chondrule spectrum is from Yesiltas et al. (2020). Spectra are normalized and offset for comparison.

4.1. Olivine

The members of group 1 are spectra A, D, and B. Spatially, points A and B exist on the inner portion of the chondrule exposure, ∼1–1.5 μm from the chondrule-matrix boundary, while point B is on the chondrule rim. The amplitude spectra of these points are dissimilar; spectra A and B have sharp, well-defined reflectance features while spectrum D has weaker and broader features. However, all three spots have spectral features at similar positions. Furthermore, when we observe the phase spectra of each position the relationship becomes much clearer. Figure 10 shows a comparison of the amplitude and phase spectra of positions A, D, and B, as well as nano-FTIR amplitude and phase spectra of single crystal enstatite (this study), forsterite (Dominguez et al., 2014), and olivine chondrule spectra from Yesiltas et al. (2020). The phase spectra of points A and D have prominent features around 925, 960, and 985 cm^{-1}, suggesting that the material these spectra represent are compositionally similar. The difference in strength of observed features in the amplitude spectra A and D are likely a result of local crystal orientation (Figure 11). These spectra match closely the nano-FTIR spectra of olivine in Didim (H3-5 chondrite) (Yesiltas et al., 2020). The forsterite nano-FTIR amplitude spectrum of Dominguez et al. (2014) appears different than the amplitude spectra of points A, D, and B. While the forsterite spectrum's main amplitude peaks are shifted to lower frequencies by ∼20 cm^{-1} (and up to 40 cm^{-1} for the phase spectra) compared to our point spectra, the point spectra resemble the forsterite spectrum more closely than that of the pure enstatite spectrum. Furthermore, based on the major peak positions and shapes, the amplitude spectra of points A, D, and B are also in disagreement with amplitude spectra (Dominguez et al., 2014) and emissivity spectra of pyroxenes (Hamilton, 2000). Therefore, we interpret the spectra of A, D, and B as olivine with spectral differences resulting from variable crystal orientation.

In amplitude spectrum A, we attribute features at 895 cm^{-1}, 952 cm^{-1}, 974 cm^{-1} to the asymmetric Si-O stretch (ν_3) and the 832 cm^{-1} feature to the symmetric O-Si-O stretch (ν_1) (Hamilton, 2010; Reynard, 1991). While identifying olivine as the material observed at points A, D, and B is relatively straightforward, understanding
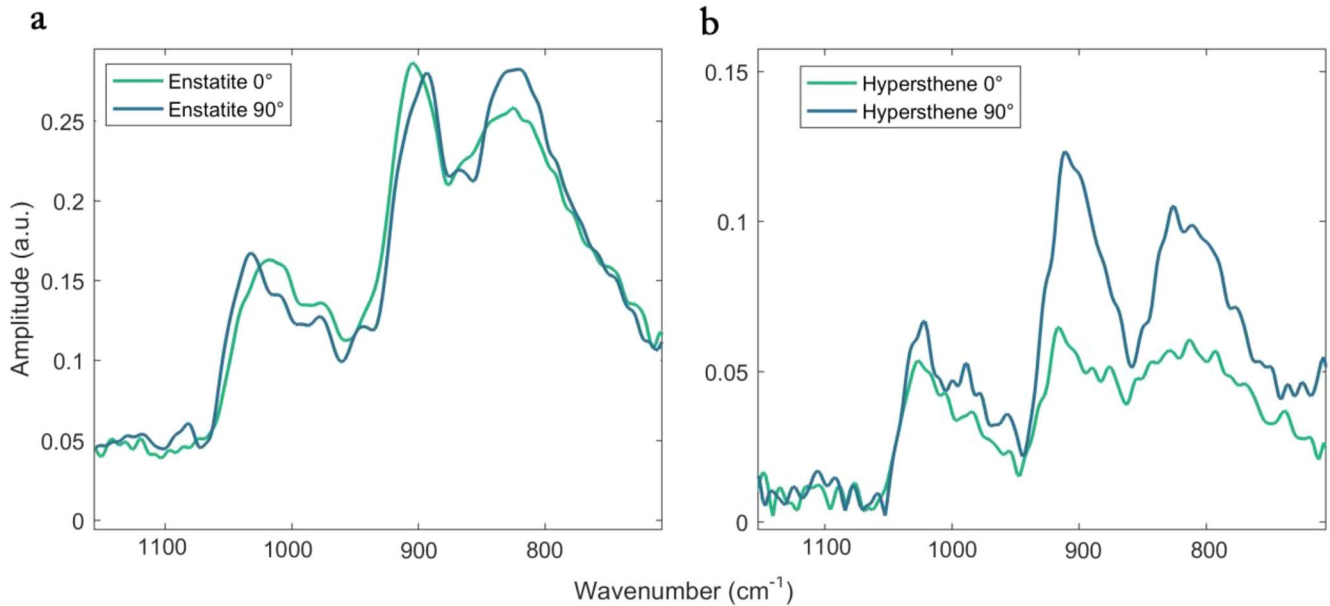
Figure 11. (a) Nano-Fourier transform infrared (Nano-FTIR) amplitude spectra of single-crystal enstatite; These spectra were collected from the same crystallographic face (a-face) but offset by a 90° rotation. (b) Nano-FTIR amplitude spectra of a single-crystal hypersthene; These spectra were collected from the same crystallographic face (a-face) but offset by a 90° rotation; Both spectral pairs demonstrate that changing crystal orientation can cause shifts in band position and strength.

exact forsterite-fayalite composition is less so. Chondrules in CM chondrites are observed to have Fe/Mg ratio values < 0.4 (Friend et al., 2016; Hezel & Palme, 2010; Palme et al., 2015), likely resulting from the high resistance of Mg-rich silicates to aqueous alteration (Zolensky et al., 1993). This suggests that the sample olivine is forsteritic in composition. However, chondrule rims and zones 4–15 μm from the rims of chondrules once subjected to aqueous alteration processes have been observed to have significant Mg depletion compared to the chondrule core (Kereszturi et al., 2014, 2015). A large body of both experimental and modeling work investigating the MIR spectral properties of the forsterite-fayallite olivine solid solution has been conducted (Burns & Huggins, 1972; Dorschner et al., 1995; Duke & Stephens, 1964; Dyar et al., 2009; Fabian et al., 2001; Hamilton, 2010; Lane et al., 2011). Collectively, these works demonstrate that there is a relationship between the peak positions of various MIR spectral bands and the ratio of Mg/Fe cations that fill the olivine M1 and M2 sites.

Lane et al. (2011), produced several, highly correlative ($R^2 \geq 0.9$) linear functions describing the relationship between a spectral band's peak position and the forsterite content of an olivine sample using conventional far-field infrared spectroscopy. Applying these functions on the amplitude spectra of points A and D would suggest that the represented material is an Fo_{70}–Fo_{90} olivine. It's clear from this body of literature that the MIR behavior of olivine spectra also depends on the cationic impurity and crystallographic orientation of a sample. Crystallite sizes of olivine may also effect the spectral band positions (Hamilton et al., 2020), with the main Si-O stretching band near ~900 cm^{-1} shifted to lower frequencies for finely crystalline olivine. Indeed, comparison of the same spectra with Hamilton et al. (2020) indicates relatively less forsteritic composition (Fo_{35}–Fo_{60}). Furthermore, the strong electromagnetic coupling between the sample and the AFM tip distorts the vibrational modes of a sample, resulting in shifts of band positions and changes in band shape. As a result, our interpretation should be treated with caution.

4.2. Spectral Anisotropy

Figure 11 shows two examples of the dependance of nano-FTIR spectra on crystallographic orientation. This figure displays four spectra; two collected from a single enstatite crystal and two collected from a single hypersthene crystal. In both cases the crystal was oriented, so the IR source was normal to the crystallographic a-face but separated by a 90° rotation with respect to the normal vector of the a-face. For both minerals, rotation by 90° leads to shifts in band position of the mineral's MIR features. Changing the orientation of the crystal can also
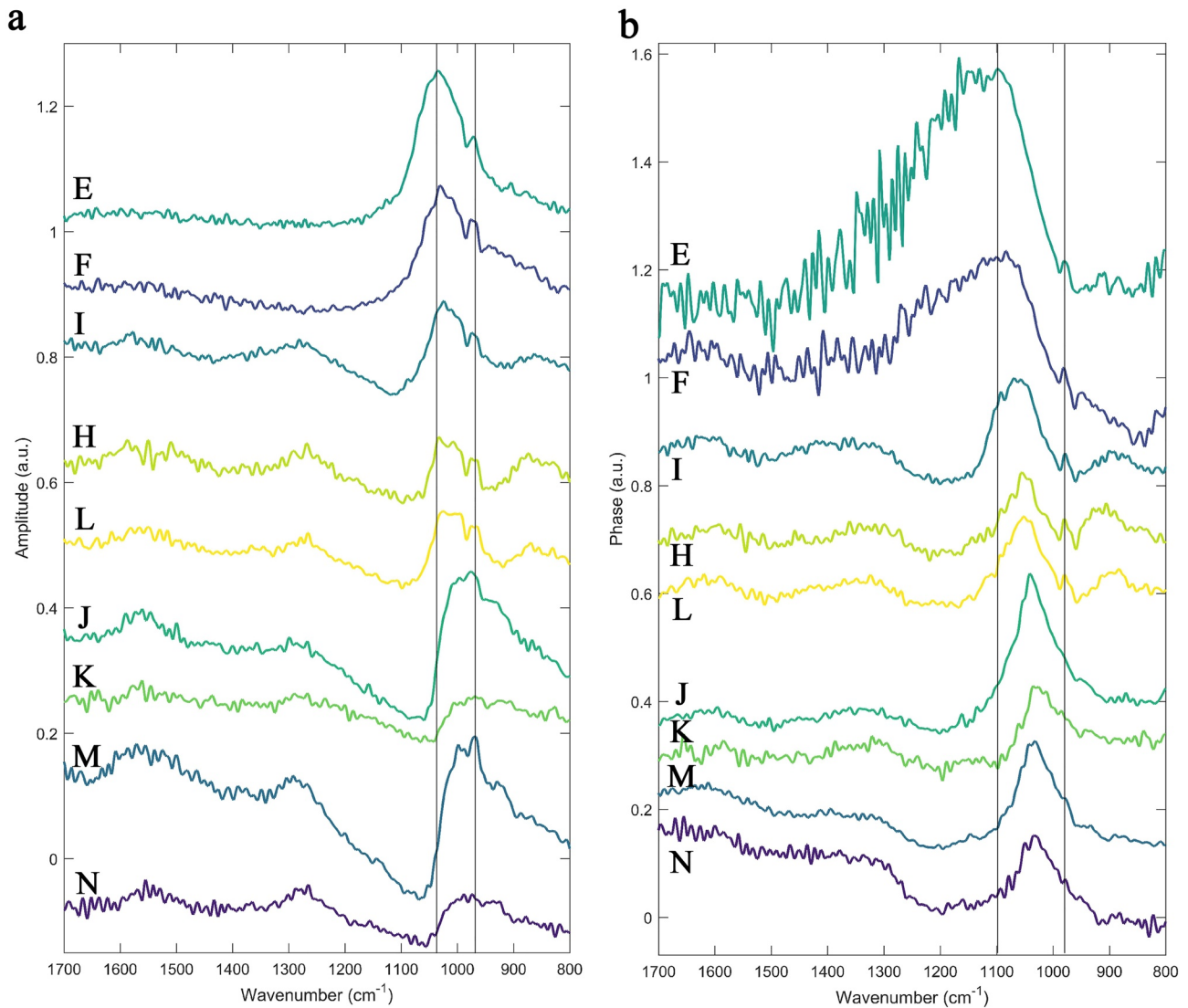
Figure 12. (a) Amplitude and (b) phase spectra of points E, F, H, I, J, K, L, M, and N; Spectra are normalized and arranged by the position of the major feature, from lowest to highest wavenumber for comparison.

diminish the strength of a given feature. The difference in strength of features in the two hypersthene spectra is similar to the difference observed between the features of amplitude spectra A, D, and B. The crystal orientation along with cation impurity and material form further obfuscate the role of Mg/Fe in the positions of olivine nano-FTIR spectra. Further investigation into the relative importance of these variables is required.

4.3. Phyllosilicates

The other major position group, Group 2, has the most members: points L, H, K, J, E, I, M, F, and N. Most of the points are in the fine-grained matrix or the suspended grains therein, but points E and F are located in the bottom right corner zone of the chondrule exposure. While band feature strength and exact position vary, each spectrum has a prominent amplitude maximum between $\sim$990 and 1,010 cm^{-1} and an ancillary feature $\sim$940–970 cm^{-1} (Figure 12a). The vertical black line clearly shows the spectral shift of the main silicate band from 990 to 1,010 cm^{-1}. The phase spectra are largely in agreement as well, with each spectrum having one main prominent feature between 1,040 and 1,100 cm^{-1}. A small feature at $\sim$970 cm^{-1} is also observed in some spectra. Based on the general position of the main absorption feature in the observed phase spectra, the materials that these points

represent are likely hydrous phyllosilicate minerals. The main phyllosilicate band, which is caused by Si–O stretching vibrations in the SiO_4 molecules composing the mineral's tetrahedral sheet, occurs $\sim$1,000–1,100 cm^{-1} (Brindley & Zussman, 1959). This is a reasonable assignment, as ALH 83100 has been observed to be composed of $\sim$85% hydrous phyllosilicates (Howard et al., 2011) and the observed amplitude spectra are consistent with reflectance spectra of previous measurements of ALH 83100 (Lindgren et al., 2020). Furthermore, we have shown the area surrounding the observed chondrule is rich in OH bearing material (Figure 1). The exact phyllosilicate observed in each spectrum is debatable, however we limit possible phases to those readily observed in CM2 chondrites.

The Mg-rich serpentines (chrysotile, antigorite, lizardite) and Fe-cronstedtite are observed in both matrix and the rims of chondrules in CM2 chondrites (Zega & Buseck, 2003; Velbel & Palmer, 2011) and make up $\sim$62 and $\sim$20–24 vol % of ALH 83100 respectively (Howard et al., 2011; Lindgren et al., 2020). Far-field MIR spectra of cronstedtite and cronstedtite-rich mixtures are largely in disagreement with the spectra of points E, I, and F shown in Figure 12. (Bates et al., 2020; Breitenfeld et al., 2021). Using laboratory emissivity spectra and Kirchhoff's law (R = 1-E), we show that the amplitude spectra of points E, I, and F are in good agreement with the far-field reflectance spectrum of antigorite (Breitenfeld et al., 2021; Figure 13). In contrast, the amplitude spectra of points K, J, M and N are in poor agreement with the reflectance spectra of saponite and antigorite. However, amplitude spectra K, J, and N match up quite well with the far-field reflectance spectrum of cronstedtite (Figure 13). Finally, reflectance spectra L and H do not have exact agreement with either pure mineral phase. Rather, theses spectra appear to be intermediates of the Fe and Mg rich phyllosilicate phases.

The existence of multiple phyllosilicate phases is also supported by the observed variation in band position and overall shape of these spectra. Phase spectra K, J, M, and N have Si-O bend positions around 1,029, 1,039, 1,034, and 1,034 cm^{-1} respectively. In terms of amplitude, spectra K, J, M, and N each have a prominent maximum centered around 968, 987, 986, and 984 cm^{-1}. Phase spectra L, H, and I have their Si-O bend positions shifted to higher wavenumber (shorter wavelength) with positions $\sim$1,051, 1,052, and 1,065 cm^{-1}. These three spectra also are observed to have an additional absorption feature at $\sim$900 cm^{-1}. Amplitude spectra L, H, and I also have prominent reflectance features at 1,009, 1,016, and 1,019 cm^{-1}, respectively. Finally, phase spectra E and F have an Si-O bend feature shifted to even higher wavenumbers at $\sim$1086 and 1102 cm^{-1}. The broad shape (full-width $\sim$300 cm^{-1}) of this feature in phase spectra E and F contrasts with the relatively thin/sharp features observed in the other phase spectra of this group.

The spectral differences observed within this group of spectra are spatially distributed, agreeing well with zones of optical amplitude variation observed in the 982 cm^{-1} map displayed in Figure 4. The position of the Si-O bend feature, in both amplitude and phase spectra, shifts to lower wavenumber as distance from the chondrule rim grows. The respective Si-O features of spectra E and F have the highest wavenumber positions and were collected from the chondrule rim. Spectra L, H, and I have intermediate wavenumber positions of their Si-O bending feature and were collected from the zone of intermediate optical amplitude (orange colored matrix) of the 10.17 μm map. Finally, spectra K, J, M, and N have the lowest wavenumber values of their Si-O bending feature and were collected from the broad zone of high optical amplitude in the 982 cm^{-1} map. We plot and compare the band position parameters of both phase and amplitude spectra in Figure 14, which shows a strong second order polynomial correlation ($y = 0.019x^2 - 37.124x + 1917$) between the Si-O bending feature band positions observed in phase and amplitude spectra for a given point. We include the Si-O bending feature's band position from the reflectance spectrum of pure cronstedtite and antigorite, seen in Figure 15, to show that the spectra appear to exist on a continuum between the two pure mineral phases. We also show the spatial distribution of the points of interest as colored fields in Figure 14. This figure shows that the points with spectra most in agreement with cronstedtite exist furthest from the chondrule rim and spectra most like antigorite exist close to or on the chondrule rim. As such, these data provide evidence for variable Fe-Mg enrichment/depletion zoning around the chondrule rim. Such evidence (Mg-rich/Fe-poor vs. Mg-poor/Fe-rich parts of the rim) suggests that aqueous alteration experienced by ALH 83100 may have occurred in the parent body as well as in the solar nebula, though it is difficult to differentiate the two origins for the alteration as aqueous alteration in the parent body can simply erase the signatures of nebular alteration. Nebular alteration results in the mixing of different phyllosilicate components (Brearley & Geiger, 1991), similar to what is observed in this study for ALH 83100. Some CO3 chondrites also exhibit mixtures of phyllosilicates within their matrices (Brearley, 1990, 1991). It is also possible that the compositional heterogeneities observed in the phyllosilicates in ALH 83100 are the result of sampling of different populations
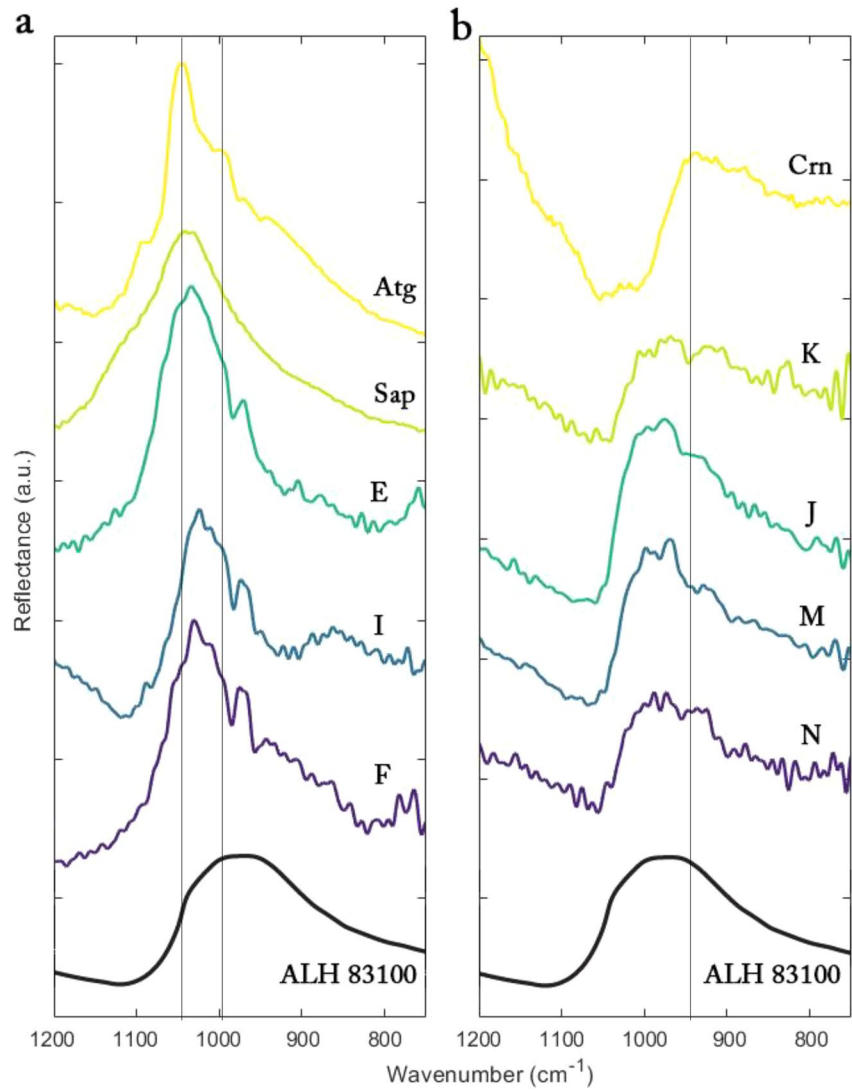
Figure 13. (a) Reflectance spectrum of pure antigorite and saponite pellets (Breitenfeld et al., 2021) and the amplitude spectra of points E, I, and F. (b) Reflectance spectrum of pure cronstedtite (Breitenfeld et al., 2021) and amplitude spectra of points K, J, M, and N; Spectrum Allan Hills 83100 reproduced from (Lindgren et al., 2020). Spectra are normalized and offset for comparison.

of nebular material such that the primary phases that underwent aqueous alteration were different (e.g., Abreu & Brearley, 2011). Aqueous alteration is known to be heterogeneous, especially at submicron scales (Abreu, 2016; Chizmadia & Brearley, 2008; Palmer & Lauretta, 2011). In this case, different parts of the rim would undergo heterogeneous alteration and result in the phyllosilicate heterogeneities as observed in ALH 83100. Additional investigations of chondrule rims in this and other CI/CM meteorites need to be conducted to provide a better constraint on the origin of alteration for the rims.

4.4. Periodic Features

All discussion thus far has considered spectral features within the wavenumber range of ~800–1,200 cm^{-1}. The low wavenumber cutoff is due to the MCT detector used in this work. However, in higher wavenumber region of our amplitude spectra, broad but well-defined features around 1,250, 1,560, 2,300, and 2,600 cm^{-1} are observed (Figure 15). For phase spectra, features are seen around 1,340, 1,600, 1,850, and 2,375, and 2,650 cm^{-1} can
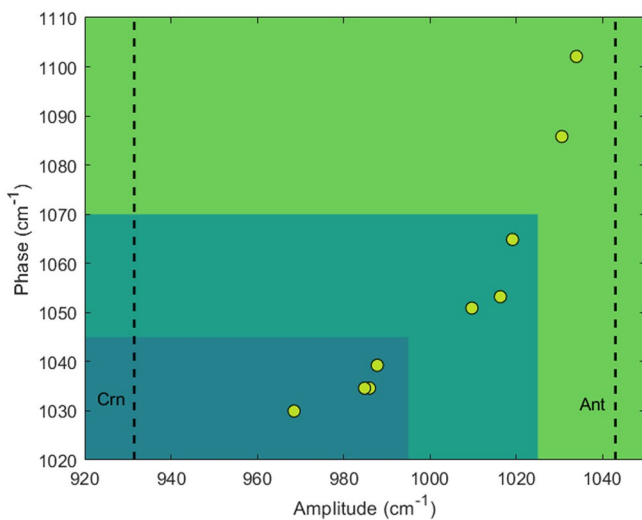
Figure 14. Phase position versus amplitude position of the Si–O bending feature observed in the spectra of points L, H, K, J, E, I, M, F, and N. Spectral parameters of these points are represented as yellow markers. Black dashed lines represent the values of the Si–O bend feature band positions observed in the reflectance spectra of pure cronstedtite (Crn) and pure antigorite (Ant). Color zones indicate the spatial distribution of collected spectra in reference to the chondrule rim; Light green (upper-right) zone represents points collected on the rim of the chondrule (E and F); Dark green (middle) zone represent points collected from an intermediate distance from the chondrule (L, H, and I); Blue (bottom-left) zone represents points collected from a relatively large distance (>2 μm) from chondrule rim. The spatial correlation of compositionally similar materials suggests variable Fe-Mg enrichment/depletion levels with respect to distance from the chondrule rim.

be observed in certain spectra. However, it remains unclear whether these features correspond to actual molecular vibrations or are artifacts introduced by the nano-FTIR experimental setup.

An argument for these bands being artifacts rather than representing molecular vibrational modes is that they appear consistently in the spectra of mineral phases we've identified as structurally distinct (e.g., olivine vs. antigorite). They appear somewhat repetitive. However, this is not the case for all points; the spectra of points E and F do not have these observed features. Furthermore, the features seen at higher wavenumbers are not characteristic of silicate vibrational modes. Rather the features seen in the 1,250–3,000 range are more likely the result of carbon bond based absorptions. The C=C vibration (ν), a characteristic feature of insoluble organic matter (IOM), has a corresponding absorption at ~1,600 cm^{-1} (Orthous-Daunay et al., 2013). Furthermore, the CH_2 (δ_s) vibration has absorptions at 1,300–1,400 cm^{-1} (Fuente et al., 2003). As carbonaceous molecules are a large component of carbonaceous chondrites, observed carbon absorption features are not a surprising result.

While there is agreement between the high wavenumber features and carbon-based absorptions, there are still issues with definitively assigning vibrational modes to the observed features. These features occur with a periodicity; starting with the 1,250 cm^{-1} feature in amplitude spectra, they continually occur ~300 cm^{-1} apart consistently. The features appear oscillatory, occurring as broad peaks with broad troughs separating them (Figure 15). Nano-FTIR has a depth sensitivity of 50–100 nm and the observed features could potentially be due to the material within the meteorite sample. This sinusoidal behavior is consistent with that of spectral interference fringes, resulting from internal reflections within thin material films (Azarfar et al., 2018; Teolis et al., 2007).

In summary, the sinusoidal features observed are likely not actual reflectance or absorption features representing a specific carbon vibration. Rather they are the result of internal reflections of light within the sample.
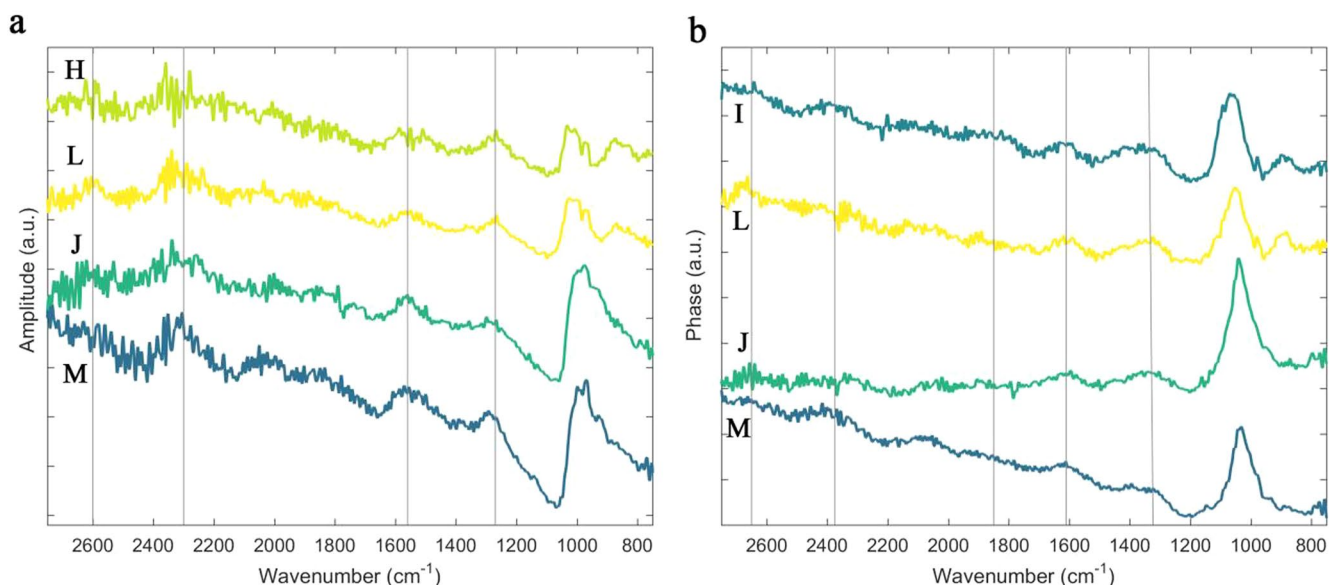

Figure 15. (a) Amplitude and (b) phase spectra of some points with features extending to the higher wavenumbers region. Vertical gray lines indicate positions of bands at higher wavenumbers.

This phenomenon makes identification of specific organic functional groups and therefore specific carbonaceous molecules difficult.

5. Conclusions

We have presented nano-FTIR images and spectra of the carbonaceous chondrite ALH 83100. From the spectra, we have identified olivine, Mg-serpentine and cronstedtite. The focused area includes a chondrule, its rim and the matrix. The spectra representing the chondrule indicates a forsteritic composition (Fo_{70-90}), while the spectra of phyllosilicate minerals within the rim and nearby matrix revealed that there is a spatial distribution of Fe-Mg enrichment/depletion surrounding the chondrule rim. This suggests a heterogeneous aqueous alteration of the rim in the parent body and hence the heterogeneous composition for the rim. Varying Fe-Mg distribution in the rim might also indicate aqueous alteration for ALH 83100 in the parent body as well as in the solar nebula.

In the context of meteoritics, nano-FTIR spectroscopy and imaging are still novel techniques. Further quantitative analyses of this and other extraterrestrial samples will be enabled by the creation of nano-FTIR mineral spectral libraries that account for crystal orientation and development of methods to address interference fringe effects. Improvements to experimental hardware, such as the introduction of multi-wavelength light sources for spectral imaging will do the same. Nanoscale investigations of the characteristic features of primitive carbonaceous chondrites, especially those like ALH 83100, which is an intermediate CM1/2 and contains signatures of varying degrees of aqueous alteration, can potentially allow us to better constrain the nebular as well as parent body processes.

Data Availability Statement

The data collected and used by this work are stored in a repository at Zenodo.org. They can be accessed at https://doi.org/10.5281/zenodo.6263235.

References

Abreu, N. M. (2016). Why is it so difficult to classify Renazzo-type (CR) carbonaceous chondrites?–Implications from TEM observations of matrices for the sequences of aqueous alteration. *Geochimica et Cosmochimica Acta*, *194*, 91–122. https://doi.org/10.1016/j.gca.2016.08.031

Abreu, N. M., & Brearley, A. J. (2011). Deciphering the nebular and asteroidal record of silicates and organic material in the matrix of the reduced CV3 chondrite Vigarano. *Meteoritics & Planetary Sciences*, *46*(2), 252–274. https://doi.org/10.1111/j.1945-5100.2010.01149.x

Alexander, C. M. D., Howard, K. T., Bowden, R., & Fogel, M. L. (2013). The classification of CM and CR chondrites using bulk H, C and N abundances and isotopic compositions. *Geochimica et Cosmochimica Acta*, *123*, 244–260. https://doi.org/10.1016/j.gca.2013.05.019

Alexander, C. M. O. D., Fogel, M., Yabuta, H., & Cody, G. D. (2007). The origin and evolution of chondrites recorded in the elemental and isotopic compositions of their macromolecular organic matter. *Geochimica et Cosmochimica Acta*, *71*(17), 4380–4403. https://doi.org/10.1016/j.gca.2007.06.052

Amarie, S., Ganz, T., & Keilmann, F. (2009). Mid-infrared near-field spectroscopy. *Optics Express*, *17*(24), 21794–21801. https://doi.org/10.1364/oe.17.021794

Amarie, S., & Keilmann, F. (2011). Broadband-infrared assessment of phonon resonance in scattering-type near-field microscopy. *Physical Review B: Condensed Matter*, *83*(4), 045404. https://doi.org/10.1103/physrevb.83.045404

Amenabar, I., Poly, S., Nuansing, W., Hubrich, E. H., Govyadinov, A. A., Huth, F., et al. (2013). Structural analysis and mapping of individual protein complexes by infrared nanospectroscopy. *Nature Communications*, *4*, 1–9. https://doi.org/10.1038/ncomms3890

Averbukh, I. S., Chernobrod, B. M., Sedletsky, O. A., & Prior, Y. (2000). Coherent near field optical microscopy. *Optics Communications*, *174*(1–4), 33–41. https://doi.org/10.1016/s0030-4018(99)00696-3

Azarfar, G., Aboualizadeh, E., Walter, N. M., Ratti, S., Olivieri, C., Norici, A., et al. (2018). Estimating and correcting interference fringes in infrared spectra in infrared hyperspectral imaging. *Analyst*, *143*(19), 4674–4683. https://doi.org/10.1039/c8an00093j

Bates, H. C., King, A. J., Donaldson Hanna, K. L., Bowles, N. E., & Russell, S. S. (2020). Linking mineralogy and spectroscopy of highly aqueously altered CM and CI carbonaceous chondrites in preparation for primitive asteroid sample return. *Meteoritics & Planetary Sciences*, *55*(1), 77–101. https://doi.org/10.1111/maps.13411

Bechtel, H. A., Johnson, S. C., Khatib, O., Muller, E. A., & Raschke, M. B. (2020). Synchrotron infrared nano-spectroscopy and-imaging. *Surface Science Reports*, *75*(3), 100493. https://doi.org/10.1016/j.surfrep.2020.100493

Brearley, A. J. (1990). Matrix mineralogy of the unequilibrated CO_3 Chondrite, ALH A77307: Evidence for disequilibrium condensation processes and implications for the origin of Chondrite matrices. *Lunar and Planetary Science*, *XXI*, 125.

Brearley, A. J. (1991). Subsolidus microstructures and cooling history of pyroxenes in the Zagami shergottite. *Lunar and Planetary Science*, *XXII*, 133.

Brearley, A. J., & Geiger, T. (1991). Mineralogical and chemical studies bearing on the origin of accretionary rims in the Murchison CM2 carbonaceous chondrite. *Meteoritics*, *26*, 323.

Breitenfeld, L. B., Rogers, A. D., Glotch, T. D., Hamilton, V. E., Christensen, P. R., Lauretta, D. S., et al. (2021). Machine learning mid-infrared spectral models for predicting modal mineralogy of CI/CM chondritic asteroids and Bennu. *Journal of Geophysical Research*, *126*(12), e2021JE007035. https://doi.org/10.1029/2021JE007035

Brindley, G. W., & Zussman, J. (1959). Infra-red absorption data for serpentine minerals. *American Mineralogist*, *44*(1–2), 185–188.

Burns, R. G., & Huggins, F. E. (1972). Cation determinative curves for Mg-Fe-Mn olivines from vibrational spectra. *American Mineralogist*, *57*, 967–985.

Chizmadia, L. J., & Brearley, A. J. (2008). Mineralogy, aqueous alteration, and primitive textural characteristics of fine-grained rims in the Y-791198 CM2 carbonaceous chondrite: TEM observations and comparison to ALHA81002. *Geochimica et Cosmochimica Acta*, *72*(2), 602–625. https://doi.org/10.1016/j.gca.2007.10.019

Chui, S. T., Chen, X., Liu, M., Lin, Z., & Zi, J. (2018). Scattering of electromagnetic waves from a cone with conformal mapping: Application to scanning near-field optical microscope. *Physical Review B: Condensed Matter*, *97*(8), 081406. https://doi.org/10.1103/physrevb.97.081406

Clark, R. N., & Roush, T. L. (1984). Reflectance spectroscopy: Quantitative analysis techniques for remote sensing applications. *Journal of Geophysical Research*, *89*(B7), 6329–6340. https://doi.org/10.1029/jb089ib07p06329

Cvitkovic, A., Ocelic, N., & Hillenbrand, R. (2007). Analytical model for quantitative prediction of material contrasts in scattering-type near-field optical microscopy. *Optics Express*, *15*(14), 8550. https://doi.org/10.1364/oe.15.008550

De Leuw, S., Rubin, A. E., Schmitt, A. K., & Wasson, J. T. (2009). *Mn-Cr systematics for the CM2. 1 chondrites QUE 93005 and ALH 83100: Implications for the timing of aqueous alteration*. Lunar Planet. Sci. XL. abstract 1794.

De Leuw, S., Rubin, A. E., & Wasson, J. T. (2010). Carbonates in CM chondrites: Complex formational histories and comparison to carbonates in CI chondrites. *Meteoritics & Planetary Sciences*, *45*(4), 513–530. https://doi.org/10.1111/j.1945-5100.2010.01037.x

Dominguez, G., Gainsforth, Z., Amano, K., Kagawa, E., Matsumoto, M., Fujioka, Y., et al. (2022). Nano-IR imaging and spectroscopy of a Ryugu asteroid sample. *Lunar and Planetary Science*, *LIII*. abstract 2736.

Dominguez, G., Mcleod, A. S., Gainsforth, Z., Kelly, P., Bechtel, H. A., Christensen, F., et al. (2014). Nanoscale infrared spectroscopy as a non-destructive probe of extraterrestrial samples. *Nature Communications*, *5*, 1–10. https://doi.org/10.1038/ncomms6445

Dorschner, J., Begemann, B., Henning, T., Jaeger, C., & Mutschke, H. (1995). Steps toward interstellar silicate mineralogy. II. Study of Mg-Fe-silicate glasses of variable composition. *Astronomy and Astrophysics*, *300*, 503.

Duke, D. A., & Stephens, J. D. (1964). Infrared investigation of the olivine group minerals. *American Mineralogist*, *49*, 1388–1406.

Dürig, U., Pohl, D. W., & Rohner, F. (1986). Near-field optical-scanning microscopy. *Journal of Applied Physics*, *59*(10), 3318–3327. https://doi.org/10.1063/1.336848

Dyar, M. D., Sklute, E. C., Menzies, O. N., Bland, P. A., Lindsley, D., Glotch, T., et al. (2009). Spectroscopic characteristics of synthetic olivine: An integrated multi-wavelength and multi-technique approach. *American Mineralogist*, *94*(7), 883–898. https://doi.org/10.2138/am.2009.3115

Elsila, J. E., Charnley, S. B., Burton, A. S., Glavin, D. P., & Dworkin, J. P. (2012). Compound-specific carbon, nitrogen, and hydrogen isotopic ratios for amino acids in CM and CR chondrites and their use in evaluating potential formation pathways. *Meteoritics & Planetary Sciences*, *47*(9), 1517–1536. https://doi.org/10.1111/j.1945-5100.2012.01415.x

Fabian, D., Henning, T., Jäger, C., Mutschke, H., Dorschner, J., & Wehrhan, O. (2001). Steps toward interstellar silicate mineralogy-VI. Dependence of crystalline olivine IR spectra on iron content and particle shape. *Astronomy & Astrophysics*, *378*(1), 228–238. https://doi.org/10.1051/0004-6361:20011196

Farrand, W. H., Wright, S. P., Glotch, T. D., Schröder, C., Sklute, E. C., & Dyar, M. D. (2018). Spectroscopic examinations of hydro-and glacio-volcanic basaltic tuffs: Modes of alteration and relevance for Mars. *Icarus*, *309*, 241–259. https://doi.org/10.1016/j.icarus.2018.03.005

Farrand, W. H., Wright, S. P., Rogers, A. D., & Glotch, T. D. (2016). Basaltic glass formed from hydrovolcanism and impact processes: Characterization and clues for detection of mode of origin from VNIR through MWIR reflectance and emission spectroscopy. *Icarus*, *275*, 16–28. https://doi.org/10.1016/j.icarus.2016.03.027

Friedlander, L. R., Glotch, T. D., Bish, D. L., Dyar, M. D., Sharp, T. G., Sklute, E. C., & Michalski, J. R. (2015). Structural and spectroscopic changes to natural nontronite induced by experimental impacts between 10 and 40 GPa. *Journal of Geophysical Research: Planets*, *120*(5), 888–912. https://doi.org/10.1002/2014je004638

Friend, P., Hezel, D. C., Barrat, J. A., Zipfel, J., & Palme, H. (2016). The chemical composition of matrix, chondrules and bulk meteorite of the CM chondrite Jbilet Winselwan. *Lunar and Planetary Science*, *XLVII*. abstract 1893.

Fuente, E., Menéndez, J. A., Díez, M. A., Suárez, D., & Montes-Morán, M. A. (2003). Infrared spectroscopy of carbon materials: A quantum chemical study of model compounds. *The Journal of Physical Chemistry B*, *107*(26), 6350–6359. https://doi.org/10.1021/jp027482g

Gillespie, A. R., Kahle, A. B., & Walker, R. E. (1986). Color enhancement of highly correlated images. 1. Decorrelation and his contrast stretches. *Remote Sensing of Environment*, *20*(3), 209–235. https://doi.org/10.1016/0034-4257(86)90044-1

Glotch, T. D., Young, J. M., Yao, Z., Bechtel, H. A., Christensen, P. R., & Lauretta, D. S. (2019). Near-field infrared spectroscopy as a tool for analysis of Chondritic returned samples. *LPI Contribution*, *2189*, 2061.

Hamilton, V. E. (2000). Thermal infrared emission spectroscopy of the pyroxene mineral series. *Journal of Geophysical Research*, *105*(E4), 9701–9716. https://doi.org/10.1029/1999je001112

Hamilton, V. E. (2010). Thermal infrared (vibrational) spectroscopy of Mg–Fe olivines: A review and applications to determining the composition of planetary surfaces. *Geochemistry*, *70*(1), 7–33. https://doi.org/10.1016/j.chemer.2009.12.005

Hamilton, V. E., Christensen, P. R., Kaplan, H. H., Haberle, C. W., Rogers, A. D., Glotch, T. D., et al. (2021). Evidence for limited compositional and particle size variation on asteroid (101955) Bennu from thermal infrared spectroscopy. *Astronomy & Astrophysics*, *650*, A120. https://doi.org/10.1051/0004-6361/202039728

Hamilton, V. E., Haberle, C. W., & Mayerhöfer, T. G. (2020). Effects of small crystallite size on the thermal infrared (vibrational) spectra of minerals. *American Mineralogist*, *105*(11), 1756–1760. https://doi.org/10.2138/am-2020-7602

Hamilton, V. E., Simon, A. S., Christensen, P. R., Reuter, D. C., Clark, B. E., Barucci, M. A., et al. (2019). Evidence for widespread hydrated minerals on asteroid (101955) Bennu. *Nature Astronomy*, *3*(4), 332–340. https://doi.org/10.1038/s41550-019-0722-2

Hanna, R. D., Hamilton, V. E., Haberle, C. W., King, A. J., Abreu, N. M., & Friedrich, J. M. (2020). Distinguishing relative aqueous alteration and heating among CM chondrites with IR spectroscopy. *Icarus*, *346*, 113760. https://doi.org/10.1016/j.icarus.2020.113760

Hapke, B. (1981). Bidirectional reflectance spectroscopy: 1. Theory. *Journal of Geophysical Research*, *86*(B4), 3039–3054. https://doi.org/10.1029/jb086ib04p03039

Hezel, D. C., & Palme, H. (2010). The chemical relationship between chondrules and matrix and the chondrule matrix complementarity. *Earth and Planetary Science Letters*, *294*(1–2), 85–93. https://doi.org/10.1016/j.epsl.2010.03.008

Hillenbrand, R., & Keilmann, F. (2000). Complex optical constants on a subwavelength scale. *Physical Review Letters*, *85*(14), 3029–3032. https://doi.org/10.1103/physrevlett.85.3029

Hillenbrand, R., Taubner, T., & Keilmann, F. (2002). Phonon-enhanced light-matter interaction at the nanometre scale. *Nature*, *418*(6894), 159–162. https://doi.org/10.1038/nature00899

Howard, K. T., Benedix, G. K., Bland, P. A., & Cressey, G. (2011). Modal mineralogy of CM chondrites by X-ray diffraction (PSD-XRD): Part 2. Degree, nature and settings of aqueous alteration. *Geochimica et Cosmochimica Acta*, *75*(10), 2735–2751. https://doi.org/10.1016/j.gca.2011.02.021

Hunt, G. R., & Salisbury, J. W. (1970). Visible and near infrared spectra of minerals and rocks. I. Silicates. *Modern Geology*, *2*, 23–30.

Jaret, S. J., Johnson, J. R., Sims, M., DiFrancesco, N., & Glotch, T. D. (2018). Microspectroscopic and petrographic comparison of experimentally shocked albite, andesine, and bytownite. *Journal of Geophysical Research: Planets*, *123*(7), 1701–1722. https://doi.org/10.1029/2018je005523

Jaret, S. J., Woerner, W. R., Phillips, B. L., Ehm, L., Nekvasil, H., Wright, S. P., & Glotch, T. D. (2015). Maskelynite formation via solid-state transformation: Evidence of infrared and X-ray anisotropy. *Journal of Geophysical Research: Planets*, *120*(3), 570–587. https://doi.org/10.1002/2014je004764

Jiang, B.-Y., Zhang, L. M., Castro Neto, A. H., Basov, D. N., & Fogler, M. M. (2016). Generalized spectral method for near-field optical microscopy. *Journal of Applied Physics*, *119*(5), 054305. https://doi.org/10.1063/1.4941343

Johnson, J. R., Jaret, S. J., Glotch, T. D., & Sims, M. (2020). Raman and infrared microspectroscopy of experimentally shocked basalts. *Journal of Geophysical Research: Planets*, *125*(2), e2019JE006240. https://doi.org/10.1029/2019JE006240

Johnson, P. E., Smith, M. O., Taylor-George, S., & Adams, J. B. (1983). A semiempirical method for analysis of the reflectance spectra of binary mineral mixtures. *Journal of Geophysical Research*, *88*(B4), 3557–3561. https://doi.org/10.1029/jb088ib04p03557

Kaplan, H. H., Lauretta, D. S., Simon, A. A., Hamilton, V. E., DellaGiustina, D. N., Golish, D. R., et al. (2020). Bright carbonate veins on asteroid (101955) Bennu: Implications for aqueous alteration history. *Science*, *370*(6517), eabc3557. https://doi.org/10.1126/science.abc3557

Kebukawa, Y., Kobayashi, H., Urayama, N., Baden, N., Kondo, M., Zolensky, M. E., & Kobayashi, K. (2019). Nanoscale infrared imaging analysis of carbonaceous chondrites to understand organic-mineral interactions during aqueous alteration. *Proceedings of the National Academy of Sciences*, *116*(3), 753–758. https://doi.org/10.1073/pnas.1816265116

Kereszturi, A., Blumberger, Z., Józsa, S., May, Z., Müller, A., Szabó, M., & Tóth, M. (2014). Alteration processes in the CV chondrite parent body based on analysis of NWA 2086 meteorite. *Meteoritics & Planetary Sciences*, *49*(8), 1350–1364. https://doi.org/10.1111/maps.12336

Kereszturi, A., Gyollai, I., & Szabó, M. (2015). Case study of chondrule alteration with IR spectroscopy in NWA 2086 CV3 meteorite. *Planetary and Space Science*, *106*, 122–131. https://doi.org/10.1016/j.pss.2014.12.015

King, A. J., Solomon, J. R., Schofield, P. F., & Russell, S. S. (2015). Characterising the CI and CI-like carbonaceous chondrites using thermogravimetric analysis and infrared spectroscopy. *Earth Planets and Space*, *67*(1), 1–12. https://doi.org/10.1186/s40623-015-0370-4

King, T. V., & Ridley, W. I. (1987). Relation of the spectroscopic reflectance of olivine to mineral chemistry and some remote sensing implications. *Journal of Geophysical Research*, *92*(B11), 11457–11469. https://doi.org/10.1029/jb092ib11p11457

Kitazato, K., Milliken, R. E., Iwata, T., Abe, M., Ohtake, M., Matsuura, S., et al. (2019). The surface composition of asteroid 162173 Ryugu from Hayabusa2 near-infrared spectroscopy. *Science*, *364*(6437), 272–275. https://doi.org/10.1126/science.aav7432

Labardi, M., Patane, S., & Allegrini, M. (2000). Artifact-free near-field optical imaging by apertureless microscopy. *Applied Physics Letters*, *77*(5), 621–623. https://doi.org/10.1063/1.127064

Lane, M. D., & Christensen, P. R. (1997). Thermal infrared spectroscopy of anhydrous carbonates. *Journal of Geophysical Research*, *102*(E11), 25581–25592. https://doi.org/10.1029/97je02046

Lane, M. D., Glotch, T. D., Dyar, M. D., Pieters, C. M., Klima, R., Hiroi, T., et al. (2011). Midinfrared spectroscopy of synthetic olivines: Thermal emission, specular and diffuse reflectance, and attenuated total reflectance studies of forsterite to fayalite. *Journal of Geophysical Research*, *116*(E8), E08010. https://doi.org/10.1029/2010je003588

Lauretta, D. S., DellaGiustina, D. N., Bennett, C. A., Golish, D. R., Becker, K. J., Balram-Knutson, S. S., et al. (2019). The unexpected surface of asteroid (101955) Bennu. *Nature*, *568*(7750), 55–60. https://doi.org/10.1038/s41586-019-1033-6

Lindgren, P., Lee, M. R., Sparkes, R., Greenwood, R. C., Hanna, R. D., Franchi, I. A., et al. (2020). Signatures of the post-hydration heating of highly aqueously altered CM carbonaceous chondrites and implications for interpreting asteroid sample returns. *Geochimica et Cosmochimica Acta*, *289*, 69–92. https://doi.org/10.1016/j.gca.2020.08.021

Mathurin, J., Dartois, E., Dazzi, A., Deniset-Besseau, A., Bejach, L., Engrand, C., et al. (2022). Nanometre-scale infrared chemical imaging (AFM-IR) study of Ryugu samples returned by the Hayabusa2 space mission. *Lunar and Planetary Science*, *LIII*. abstract 2142.

McLeod, A. S., Kelly, P., Goldflam, M. D., Gainsforth, Z., Westphal, A. J., Dominguez, G., et al. (2014). Model for quantitative tip-enhanced spectroscopy and the extraction of nanoscale-resolved optical constants. *Physical Review B: Condensed Matter*, *90*(8), 085136. https://doi.org/10.1103/physrevb.90.085136

Miyamoto, M., & Zolensky, M. E. (1994). Infrared diffuse reflectance spectra of carbonaceous chondrites: Amount of hydrous materials. *Meteoritics*, *29*(6), 849–853. https://doi.org/10.1111/j.1945-5100.1994.tb01098.x

Mustard, J. F., & Pieters, C. M. (1987). Quantitative abundance estimates from bidirectional reflectance measurements. *Journal of Geophysical Research*, *92*(B4), 617–626. https://doi.org/10.1029/jb092ib04p0e617

Nasse, M. J., Walsh, M. J., Mattson, E. C., Reininger, R., Kajdacsy-Balla, A., Macias, V., et al. (2011). High-resolution Fourier-transform infrared chemical imaging with multiple synchrotron beams. *Nature Methods*, *8*(5), 413–416. https://doi.org/10.1038/nmeth.1585

Orthous-Daunay, F. R., Quirico, E., Beck, P., Brissaud, O., Dartois, E., Pino, T., & Schmitt, B. (2013). Mid-infrared study of the molecular structure variability of insoluble organic matter from primitive chondrites. *Icarus*, *223*(1), 534–543. https://doi.org/10.1016/j.icarus.2013.01.003

Palme, H., Hezel, D. C., & Ebel, D. S. (2015). The origin of chondrules: Constraints from matrix composition and matrix-chondrule complementarity. *Earth and Planetary Science Letters*, *411*, 11–19. https://doi.org/10.1016/j.epsl.2014.11.033

Palmer, E. E., & Lauretta, D. S. (2011). Aqueous alteration of kamacite in CM chondrites. *Meteoritics & Planetary Sciences*, *46*(10), 1587–1607. https://doi.org/10.1111/j.1945-5100.2011.01251.x

Pearson, V. K., Sephton, M. A., Kearsley, A. T., Bland, P. A., Franchi, I. A., & Gilmour, I. (2002). Clay mineral-organic matter relationships in the early solar system. *Meteoritics & Planetary Sciences*, *37*(12), 1829–1833. https://doi.org/10.1111/j.1945-5100.2002.tb01166.x

Reynard, B. (1991). Single-crystal infrared reflectivity of pure Mg_2SiO_2 forsterite and $(Mg_{0.86}, Fe_{0.14})_2SiO_4$ olivine. *Physics and Chemistry of Minerals*, *18*(1), 19–25. https://doi.org/10.1007/bf00199039

Shirley, K. A., & Glotch, T. D. (2019). Particle size effects on mid-infrared spectra of lunar analog minerals in a simulated lunar environment. *Journal of Geophysical Research: Planets*, *124*(4), 970–988. https://doi.org/10.1029/2018je005533

Shkuratov, Y., Starukhina, L., Hoffman, H., & Arnold, G. (1999). A model of spectral albedo of particulate surfaces: Implications for optical properties of the Moon. *Icarus*, *137*(2), 235–246. https://doi.org/10.1006/icar.1998.6035

Simon, A. A., Kaplan, H. H., Hamilton, V. E., Lauretta, D. S., Campins, H., Emery, J. P., et al. (2020). Widespread carbon-bearing materials on near-Earth asteroid. *Bennu, Science*, *370*(6517). https://doi.org/10.1126/science.abc3522

Takir, D., Emery, J. P., Mcsween, H. Y., Jr., Hibbitts, C. A., Clark, R. N., Pearson, N., & Wang, A. (2013). Nature and degree of aqueous alteration in CM and CI carbonaceous chondrites. *Meteoritics & Planetary Sciences*, *48*(9), 1618–1637. https://doi.org/10.1111/maps.12171

Teolis, B. D., Loeffler, M. J., Raut, U., Famá, M., & Baragiola, R. A. (2007). Infrared reflectance spectroscopy on thin films: Interference effects. *Icarus*, *190*(1), 274–279. https://doi.org/10.1016/j.icarus.2007.03.023

Velbel, M. A., & Palmer, E. E. (2011). Fine-grained serpentine in CM2 carbonaceous chondrites and its implications for the extent of aqueous alteration on the parent body: A review. *Clays and Clay Minerals*, *59*(4), 416–432. https://doi.org/10.1346/ccmn.2011.0590405

Viviano-Beck, C. E., Seelos, F. P., Murchie, S. L., Kahn, E. G., Seelos, K. D., Taylor, H. W., et al. (2014). Revised CRISM spectral parameters and summary products based on the currently detected mineral diversity on Mars. *Journal of Geophysical Research: Planets*, *119*(6), 1403–1431. https://doi.org/10.1002/2014je004627

Xu, X. G., Rang, M., Craig, I. M., & Raschke, M. B. (2012). Pushing the sample-size limit of infrared vibrational nanospectroscopy: From monolayer toward single molecule sensitivity. *The Journal of Physical Chemistry Letters*, *3*(13), 1836–1841. https://doi.org/10.1021/jz300463d

Yesiltas, M., Glotch, T. D., Jaret, S. J., Verchovsky, S., & Greenwood, R. C. (2019). Carbonaceous matter in the Sarıçiçek meteorite. *Meteoritics & Planetary Science*, *54*(7), 1495–1511. https://doi.org/10.1111/maps.13287

Yesiltas, M., Glotch, T. D., & Sava, B. (2021). Nano-FTIR spectroscopic identification of prebiotic carbonyl compounds in Dominion Range 08006 carbonaceous chondrite. *Scientific Reports*, *11*(1), 11656. https://doi.org/10.1038/s41598-021-91200-8

Yesiltas, M., Hirschmugl, C. J., & Peale, R. E. (2013). In situ investigation of meteoritic organic-mineral relationships by high spatial resolution infrared spectroscopy. *Meteoritics and Planetary Science Supplement*, *76*, 5068.

Yesiltas, M., Kaya, M., Glotch, T. D., Brunetto, R., Maturilli, A., Helbert, J., & Ozel, M. E. (2020). Biconical reflectance, micro-Raman, and nano-FTIR spectroscopy of the Didim (H3-5) meteorite: Chemical content and molecular variations. *Meteoritics & Planetary Sciences*, *55*(11), 2404–2421. https://doi.org/10.1111/maps.13585

Yesiltas, M., & Kebukawa, Y. (2016). Associations of organic matter with minerals in Tagish Lake meteorite via high spatial resolution synchrotron-based FTIR microspectroscopy. *Meteoritics & Planetary Sciences*, *51*(3), 584–595. https://doi.org/10.1111/maps.12609

Yesiltas, M., Sedlmair, J., Peale, R. E., & Hirschmugl, C. J. (2017). Synchrotron-based three-dimensional Fourier-transform infrared spectro-microtomography of Murchison meteorite grain. *Applied Spectroscopy*, *71*(6), 1198–1208. https://doi.org/10.1177/0003702816671072

Zega, T. J., & Buseck, P. R. (2003). Fine-grained-rim mineralogy of the cold Bokkeveld CM chondrite. *Geochimica et Cosmochimica Acta*, *67*(9), 1711–1721. https://doi.org/10.1016/s0016-7037(02)01172-9

Zolensky, M., Barrett, R., & Browning, L. (1993). Mineralogy and composition of matrix and chondrule rims in carbonaceous chondrites. *Geochimica et Cosmochimica Acta*, *57*(13), 3123–3148. https://doi.org/10.1016/0016-7037(93)90298-b

Zolensky, M. E., Mittlefehldt, D. W., Lipschutz, M. E., Wang, M. S., Clayton, R. N., Mayeda, T. K., et al. (1997). CM chondrites exhibit the complete petrologic range from type 2 to 1. *Geochimica et Cosmochimica Acta*, *61*(23), 5099–5115. https://doi.org/10.1016/s0016-7037(97)00357-8